Evidence of a South Asian Proto-Monsoon During the Oligocene-Miocene Transition

C Beasley, S Kender, L Giosan, C T Bolton, P Anand, M J Leng, K Nilsson-kerr, C V Ullmann, S P Hesselbo, K Littler

Paleoceanography and Paleoclimatology®

AGU ADVANCING EARTH AND SPACE SCIENCE

RESEARCH ARTICLE
10.1029/2021PA004278

Evidence of a South Asian Proto-Monsoon During the Oligocene-Miocene Transition

C. Beasley[1], S. Kender[1], L. Giosan[2], C. T. Bolton[3], P. Anand[4], M. J. Leng[5], K. Nilsson-Kerr[4,6], C. V. Ullmann[1,7], S. P. Hesselbo[1,7], and K. Littler[1,7]

[1]Camborne School of Mines, University of Exeter, Penryn, UK, [2]Department of Geology and Geophysics, Woods Hole Oceanographic Institution, Woods Hole, MA, USA, [3]Aix Marseille University, CNRS, IRD, INRAE, Collège de France, CEREGE, Aix en Provence, France, [4]School of Environment, Earth and Ecosystem Sciences, Faculty of Science, Technology and Mathematics, The Open University, Milton Keynes, UK, [5]National Environmental Isotope Facility, British Geological Survey, UK and School of Biosciences, University of Nottingham, Nottingham, UK, [6]Now at Department of Earth Sciences, University of Bergen, Bergen, Norway, [7]Environment and Sustainability Institute, University of Exeter, Penryn, UK

Key Points:

- Geochemical data from eastern Arabian Sea indicate Oligocene-Miocene transition is key interval of strengthening of South Asian proto-monsoon
- Early phase of transition (23.7–23.0 Ma) displays intensification of winter monsoon-like circulation associated with global cooling
- "Deglaciation" phase (23.0–22.7 Ma) triggers the establishment of OMZ, signaling the strengthening of proto-monsoon atmospheric circulation

Supporting Information:

Supporting Information may be found in the online version of this article.

Correspondence to:

C. Beasley,
c.beasley@exeter.ac.uk

Citation:

Beasley, C., Kender, S., Giosan, L., Bolton, C. T., Anand, P., Leng, M. J., et al. (2021). Evidence of a South Asian proto-monsoon during the Oligocene-Miocene transition. *Paleoceanography and Paleoclimatology*, *36*, e2021PA004278. https://doi.org/10.1029/2021PA004278

Received 12 APR 2021
Accepted 30 AUG 2021

Abstract The geological history of the South Asian monsoon (SAM) before the Pleistocene is not well-constrained, primarily due to a lack of available continuous sediment archives. Previous studies have noted an intensification of SAM precipitation and atmospheric circulation during the middle Miocene (~14 Ma), but no records are available to test how the monsoon changed prior to this. In order to improve our understanding of monsoonal evolution, geochemical and sedimentological data were generated for the Oligocene-early Miocene (30–20 Ma) from Indian National Gas Hydrate Expedition 01 Site NGHP-01-01A in the eastern Arabian Sea, at 2,674 m water depth. We find the initial glaciation phase (23.7–23.0 Ma) of the Oligocene-Miocene transition (OMT) to be associated with an increase in water column ventilation and water mass mixing, suggesting an increase in winter monsoon type atmospheric circulation, possibly driven by a relative southward shift of the intertropical convergence zone. During the latter part of the OMT, or "deglaciation" phase (23.0–22.7 Ma), a long-term decrease in Mn (suggestive of deoxygenation), increase in Ti/Ca and dissolution of the biogenic carbonate fraction suggest an intensification of a proto-summer SAM system, characterized by the formation of an oxygen minimum zone in the eastern Arabian Sea and a relative increase of terrigenous material delivered by runoff to the site. With no evidence at this site for an active SAM prior to the OMT we suggest that changes in orbital parameters, as well as possibly changing Tethyan/Himalayan tectonics, caused this step change in the proto-monsoon system at this intermediate-depth site.

1. Introduction

Today, the Arabian Sea region is strongly influenced by the modern South Asian monsoon (SAM) or Indian monsoon system, which is a dominant vector for the transport of heat and moisture in the tropical low latitudes (Gupta et al., 2020). The initiation and intensification of the Asian monsoon systems have been hypothesized to be linked with atmospheric CO_2 levels and the uplift of the Himalayan-Tibetan Plateau (Clift et al., 2002; Farnsworth et al., 2019; Jiang et al., 2008; Kutzbach et al., 1993; Tada et al., 2016; Thomson et al., 2021), although the timing and origin of the various Asian monsoon sub-systems and the link to Himalayan-Tibetan Plateau uplift are still debated (Acosta & Huber, 2020; Boos & Kuang, 2010, 2013; Ding et al., 2017; Spicer, 2017; Thomson et al., 2021). A number of east Asian dust records suggest that the east Asian monsoon was established prior to or during the Oligocene-Miocene interval (Guo et al., 2002, 2008; Licht et al., 2016; J. Sun et al., 2010). However, there are few available, continuous sedimentary records prior to the Miocene to help constrain timing of the SAM (Betzler et al., 2016; Bialik et al., 2020; Pandey et al., 2016). The available records are dominantly terrestrial and lack sufficient age constraints to place sedimentological changes into a climatic context (Reuter et al., 2013). Thus, estimates for the initiation of the SAM range from the early Paleogene (Farnsworth et al., 2019; Licht et al., 2014) to the middle/late Miocene (Betzler et al., 2016; Bialik et al., 2020; Gupta et al., 2015; X. Yang et al., 2020). Constraining the timing of SAM initiation is important to understand the mechanisms/processes that govern it and potentially aid in refining future predictions of the monsoon associated with anthropogenic climate change.

The Oligocene to earliest Miocene (~34–22 million years ago; Ma) began with the major Eocene-Oligocene transition glaciation event (~34 Ma), thought to represent the first glaciation of Antarctica (Keigwin & Corliss, 1986; Lear et al., 2000, 2004, 2008; Scher et al., 2011; Zachos et al., 1992, 1996; Zachos & Kump, 2005), and ended with the transient Oligocene-Miocene transition (OMT) glaciation event (~23 Ma; Beddow et al., 2016; Lear et al., 2004; Mawbey & Lear, 2013; Miller et al., 1991; Pälike et al., 2006; Paul et al., 2000; Stewart et al., 2017; Wade & Pälike, 2004; Zachos, Shackleton, et al., 2001). We currently lack detailed data to infer ocean and atmosphere circulations influencing climate from the northern Indian Ocean during this enigmatic "coolhouse" interval (Westerhold et al., 2020).

During the middle Oligocene (~28–26.3 Ma) there was a transient glacial interval coined as the middle Oligocene glacial interval (MOGI; Liebrand et al., 2017). This interval consisted of unstable but generally cooler climatic conditions. During the late Oligocene (~27–24 Ma) a trend towards relative global warmth, termed the late Oligocene warming event (LOWE), seemingly occurred during a time when proxy reconstructions suggest decreasing atmospheric CO_2 (Figure 1; O'Brien et al., 2020; Zhang et al., 2013). Immediately following the LOWE is the OMT glaciation ("Mi-1" event; Miller et al., 1991). This event is marked by a 0.6–1.5‰ positive excursion in benthic foraminifera $\delta^{18}O$, thought to be caused by Antarctic ice volume expansion (Liebrand et al., 2011, 2017) and ~2°C cooling of deep waters (Lear et al., 2004; Mawbey & Lear, 2013). Sea surface temperature (SST) decreases over the same interval have also been suggested by palynological data (Egger et al., 2018), biomarker and alkenone proxies (Guitián et al., 2019; Liu et al., 2018; Super et al., 2018; Zhang et al., 2013), and modeling (Liebrand et al., 2011) for the Atlantic. However, the evolution of SST over this interval, including the magnitude of changes and spatial heterogeneity, is not well constrained (Guitián et al., 2019), with some equatorial sites showing little change in surface water oxygen isotopic values over the OMT (Figure 1; Matsui et al., 2016; Stewart et al., 2017). Accompanying this global cooling was ~50–65 m of glacioeustatic sea level fall, accommodated by significant ice growth on Antarctica (Beddow et al., 2016; Mawbey & Lear, 2013; Wade & Pälike, 2004).

The OMT is superimposed upon pronounced orbitally paced variation in ice volume/temperature with changes in $\delta^{18}O$ on the order of ~0.5‰–1‰ and in $\delta^{13}C$ of ~0.5‰ (Egger et al., 2018; Liebrand et al., 2011, 2016, 2017; Mawbey & Lear, 2013; Pälike et al., 2006; Paul et al., 2000; Wade & Pälike, 2004; Zachos et al., 2001). It has been suggested that the dominant forcing on the climate/cryosphere system through the late Oligocene to early Miocene is eccentricity modulation of precession (short and long; ~110 and ~405 kyr respectively), also with a strong imprint of the 2.4 Myr very long-period eccentricity (Figure 1; Beddow et al., 2018; De Vleeschouwer et al., 2020; Drury et al., 2020; Egger et al., 2018; Greenop et al., 2019; Liebrand et al., 2016, 2017; van Peer et al., 2020; Westerhold et al., 2020). The particular orbital configuration present during the OMT glaciation recovery phase (high amplitude oscillations of 110 kyr eccentricity) occurred a further four times throughout the Oligocene-Miocene interval (Greenop et al., 2019; Liebrand et al., 2017), associated with more minor cryosphere responses. Despite this, the OMT glaciation stands out from these cyclic events as a prominent, transient event terminating the LOWE (Liebrand et al., 2017). It is suggested that conditions promoting Antarctic glaciation across the OMT were a result of the long-term decline in atmospheric CO_2 rather than being triggered solely by changes in orbital parameters (Greenop et al., 2019). This multi-million-year decrease in pCO_2 observed in compiled $\delta^{11}B$ (Greenop et al., 2019) and alkenone records (Figure 1; Zhang et al., 2013) may be linked to the broadly contemporaneous uplift of the Himalayan-Tibetan Plateau, leading to an increase in weathering rates subsequently sequestering atmospheric CO_2 (Raymo & Ruddiman, 1992; Zachos & Kump, 2005; T. Zhang et al., 2021). Despite the proximity of the Arabian Sea to the Himalayan-Tibetan Plateau there are very few long continuous records available in this region to help constrain these hypotheses of paired tectonic and climatic change (see Clift & Webb, 2019 for a review).

Core NGHP-01-01A represents a unique opportunity to investigate Oligocene-Miocene paleoceanographic dynamics at a relatively high resolution (10–40 kyr) in an oceanographically significant but otherwise data-barren area of the Arabian Sea (Figure 2). Here we present new sedimentological and biostratigraphic data, paired planktic and benthic foraminiferal stable isotopes, planktic foraminiferal Mg/Ca ratios, and bulk sediment elemental ratios to reveal new insights into ocean and atmospheric circulation during this time interval. We show that the OMT was a fundamental turning point for the initiation/intensification of proto-SAM atmospheric and oceanographic circulation causing a significant step-change in the sedimentary record in the eastern Arabian Sea.

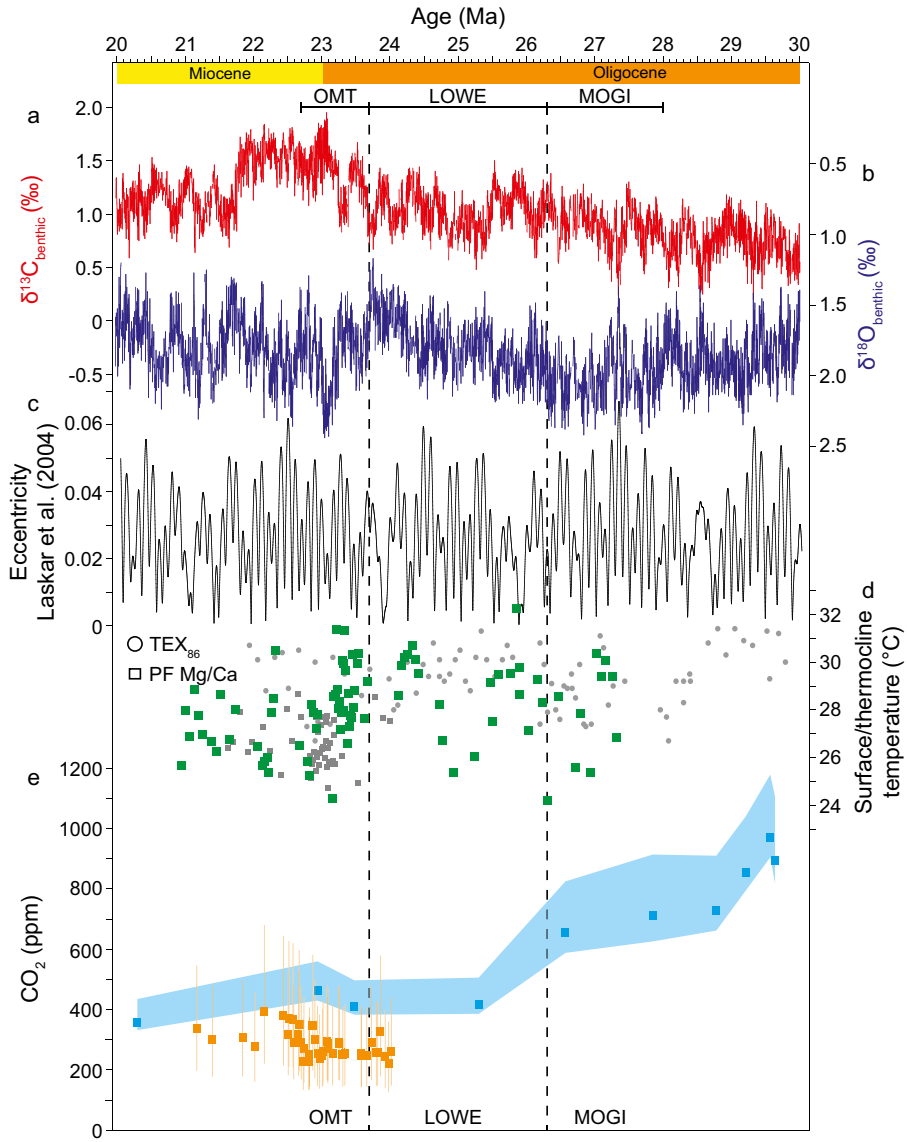

Figure 1. Summary of Oligocene-Miocene climate evolution. Abbreviations from Liebrand et al. (2017) where MOGI is the middle Oligocene glacial interval, LOWE is the late Oligocene warming event, and OMT is the Oligocene-Miocene transition. (a) and (b) Benthic foraminifera carbon ($\delta^{13}C$) (a) and oxygen ($\delta^{18}O$) (b) stable isotopes from ODP Site 1264 (Liebrand et al., 2016) in the equatorial Atlantic. (c) Eccentricity variations from Laskar et al. (2004). (d) Equatorial thermocline/sea surface temperature records from the Atlantic using TEX_{86} (gray circles, ODP Site 929; O'Brien et al., 2020) and planktic foraminiferal (PF) Mg/Ca (gray squares, ODP Site 926; Stewart et al., 2017) and this study (green squares). TEX_{86} data record sea surface temperature, whilst PF Mg/Ca records thermocline temperature. (e) Atmospheric CO_2 evolution derived from alkenone $\delta^{13}C$ in blue from ODP Site 925 (Zhang et al., 2013) and $\delta^{11}B$ in orange from ODP Site 926 in the equatorial Atlantic and ODP Site 872 in tropical north Pacific (Greenop et al., 2017, 2019). Error bars in alkenone record represent variability in temperature and phosphate estimates used to calculate CO_2 (see Zhang et al., 2013). Error bars in $\delta^{11}B$ record represent 2σ uncertainty.

2. Modern Arabian Sea Oceanography

In the modern ocean, the Arabian Sea region is dominantly influenced by the seasonal variability of the SAM subsystem represented by the South Asian summer monsoon (SASM) or Indian summer monsoon and South Asian winter monsoon (SAWM) or Indian winter monsoon. In the present day, the SAM is caused by seasonal atmospheric pressure contrasts between the Indian Ocean and adjacent Eurasian landmass (Gadgil, 2018; Schott & McCreary, 2001). During the boreal summer (SASM) moisture laden air flows from the

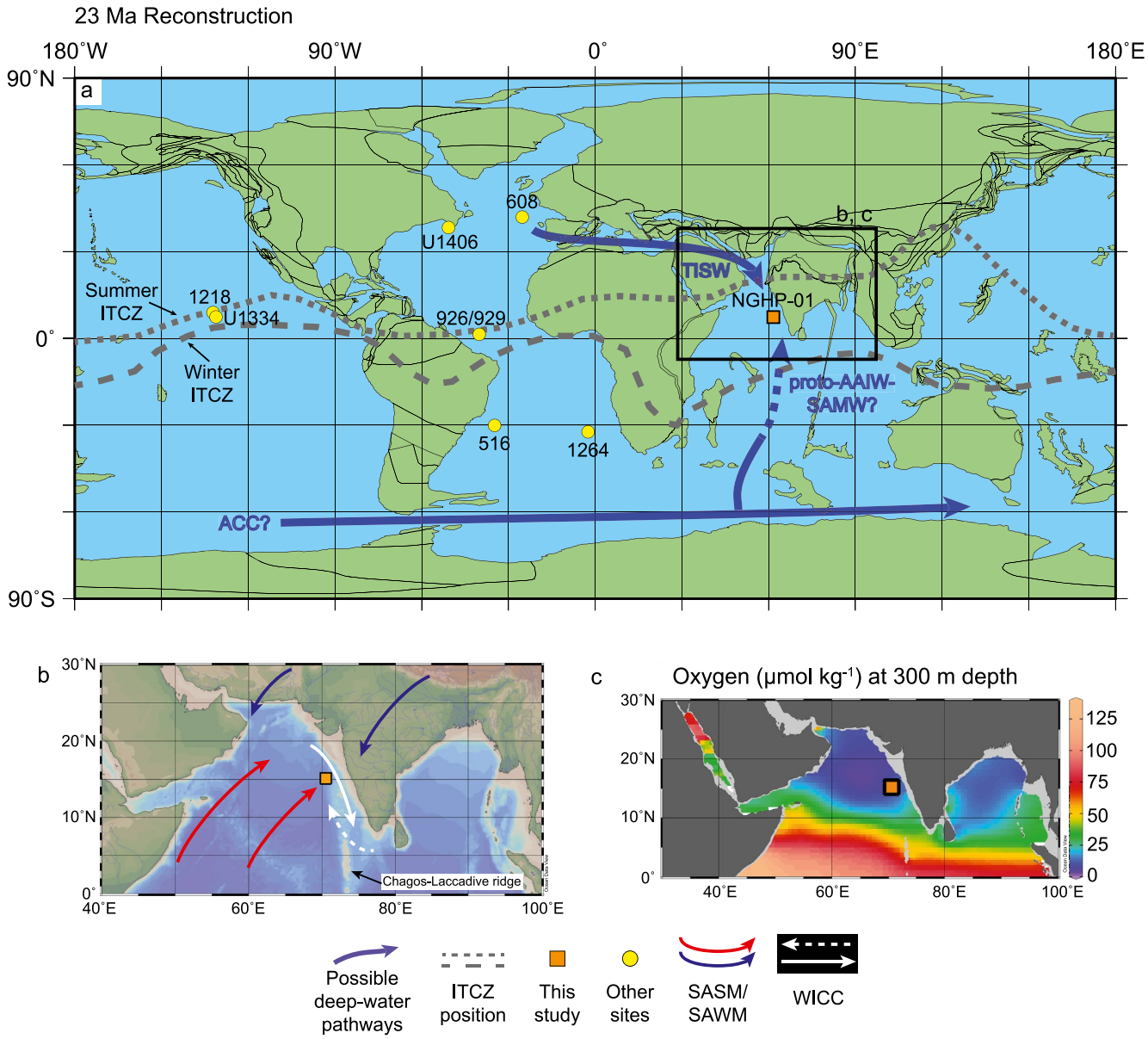

Figure 2. Location of Site NGHP-01-01A shown with orange square in all maps. (a) Paleogeographic map of ~23 Ma (Oligocene-Miocene boundary). Blue arrows show potential deep-water currents affecting the NGHP-01-01A site (e.g., Böning & Bard, 2009; Hamon et al., 2013). Dotted gray line depicts the approximate modern summer position of the ITCZ, dashed gray line shows winter ITCZ position. Yellow circles show other marine core sites containing Oligocene-Miocene aged sediments for which we have comparable geochemical data. The ACC is the Antarctic Circumpolar Current; TISW is Tethyan Indian Saline Water; AAIW-SAMW is Antarctic Intermediate and Subantarctic Mode Water. Map generated through Ocean Drilling Stratigraphic Network (OSDN) Paleomap project (https://www.odsn.de/odsn/services/paleomap/paleomap.html). (b) Modern bathymetric map expanded from black square in map (a). Red arrows show South Asian summer monsoon (SASM) winds, blue arrows show SAWM winds. The white arrows show West Indian Coast Current surface circulation during the SASM (solid line) and during the SAWM (dashed line). (c) Modern annual oxygen saturation (μmol kg^{-1}) at 300 m depth, also showing area expanded from black square in map (a). Both maps generated with Ocean Data View (Schlitzer, https://odv.awi.de, 2020) using data from World Ocean Atlas 2018.

cooler Indian Ocean (high atmospheric pressure) towards the warmer Indian landmass (low atmospheric pressure) due to the northward shift of the Intertropical Convergence Zone (ITCZ). This northward shift is controlled by heating of the Indian subcontinent combined with the Himalayan-Tibetan Plateau preventing the intrusion of cooler air from the north (Acosta & Huber, 2020; Boos & Kuang, 2010, 2013; Bordoni & Schneider, 2008; Privé & Plumb, 2007). The moisture is subsequently released as precipitation when reaching the topographic high of the Himalayas. Site NGHP-01-01A in the eastern Arabian Sea is affected by SASM

precipitation both directly and via runoff from the Western Ghats, which run as a topographic high parallel to the west Indian coast (X. Yang et al., 2020). During the SAWM (boreal winter) the atmospheric pressure gradient is reversed, with a southward shift of the ITCZ and dominant airflow from the cooler land to the warmer ocean. This results in strong, dry, north-easterly winds originating from the Indian landmass and flowing towards the Arabian Sea (Figure 2b). It is thought that the majority of lithogenic flux to the Arabian Sea occurs during the SASM from fluvial input derived from the Western Ghats; aeolian (wind blown dust) input during the SAWM constitutes a negligible percentage of mass accumulation in the eastern Arabian Sea (Clemens & Prell, 1990, 1991).

As a result of this seasonally changing atmospheric circulation, surface ocean currents also change seasonally. During the SASM surface water flow in the eastern Arabian Sea is from the north to south, via the West Indian Coast Current (Schott & McCreary, 2001). This surface water flow brings slightly higher salinity surface water from the northern Arabian Sea along the west coast of India during the SASM (Prasanna Kumar et al., 2004). During the SAWM the West Indian Coast Current switches direction and flows from south to north. These waters are sourced from the Bay of Bengal and the northern Indian Ocean and are thought to bring fresher surface waters along the west Indian coast (Prasanna Kumar et al., 2004; Schott & McCreary, 2001).

During the SASM, strong south-westerly winds along the Somali coast, known as the Somali/Findlater jet (Findlater, 1969), induce surface water currents moving away from the Arabian Peninsula and east Africa and towards western India (deflected to the right due to the Coriolis effect). This creates a strong seasonal coastal upwelling of nutrient-rich deep waters in the western Arabian Sea and resultant high surface productivity (Anderson & Prell, 1993). Seasonally high surface productivity, coupled with a poorly ventilated thermocline, induce an intense oxygen minimum zone (OMZ) in the Arabian Sea (Figure 2c), present between ~150–1,250 m depth (Lachkar et al., 2018; Reichart, Nortier, et al., 2002). Within this zone oxygen levels can be as low as 2 μM (Reichart, Nortier, et al., 2002) resulting in intense denitrification (Kim et al., 2018). Although the OMZ is present dominantly in the northeast and central Arabian Sea (Figure 2c), the area of high biological productivity is concentrated around the basin margins and especially the western part of the Arabian Sea (Acharya & Panigrahi, 2016; Lachkar et al., 2018). Site NGHP-01-01A is located within the central-eastern part of the modern OMZ.

The Arabian Sea OMZ is thought to have been at least intermittently present since the middle Miocene (Betzler et al., 2016; Bialik et al., 2020). During Pleistocene glacials, the OMZ was periodically ventilated by incursions of southern sourced Antarctic Intermediate Water and Subantarctic Mode Water (AAIW-SAMW) (Böning & Bard, 2009; Reichart, Schenau, et al., 2002). Whether similar oceanographic circulation could occur during the Oligocene-early Miocene interval, with different tectonic configuration and climate in place, is unknown as there are no published marine sediment records in the Arabian Sea prior to the early Miocene to test this (Bialik et al., 2020; Pandey et al., 2016; X. Yang et al., 2020).

3. Materials and Methods

Sediment core NGHP-01-01A from the eastern Arabian Sea (15° 18.366′N, 70° 54.192′E; Figure 2) was recovered by the RV *JOIDES Resolution* funded by the National Gas Hydrate Program (NGHP) of India Expedition-01 in 2006 from a paleodepth of ~2,250 m at 25 Ma (current water depth 2,674.2 m; see Supporting Information S1 for paleodepth calculations). The core sits on the eastern side of the Chagos-Laccadive Ridge, where the ridge meets the continental shelf (Figure 2; Collett et al., 2008). The site was consistently located above the carbonate compensation depth, which was >4,000 m during the Oligocene-Miocene interval (Campbell et al., 2018; Peterson & Backman, 1990; van Andel, 1975). The dominant lithology of the Oligocene-Miocene portion of the core is carbonate-rich pelagic ooze, dominated by nannofossil and foraminiferal components with a varying but significant clay component (~20–30 wt%; Johnson et al., 2014). The investigated interval of the core has low total organic carbon content (TOC <1%; Johnson et al., 2014). Importantly, there is no evidence of gas hydrates within the core (Collett et al., 2008); however, in order to ascertain gas hydrate content, periodic whole core samples were taken during shipboard operations leading to core-gaps throughout the study interval. Calcareous nannofossil biostratigraphy suggests continuous sedimentation across the late Oligocene-early Miocene period studied here (Flores et al., 2014 and this study).

3.1. Sampling and Sample Preparation

A total of 185 samples were taken from core NGHP-01-01A between the depths of 233.99 and 280.11 meters below sea floor (mbsf), spanning core sections 30X-1 to 35X-6. A robust calcareous nannofossil biostratigraphic age model for the site (Flores et al., 2014 and this study) shows this part of the core was deposited between the early Oligocene and early Miocene (~31.4–20 Ma). From 262 to 280 mbsf samples were taken at a resolution of ~50 cm, capturing the early/middle Oligocene. The sections 243–262 mbsf and 214–224 mbsf were sampled at a ~15 cm resolution in order to target the late Oligocene and early Miocene intervals at a higher resolution. The sections 224–243 mbsf, comprising the Oligocene-Miocene boundary, was sampled at an ~8 cm resolution.

Samples were freeze dried at −60°C and 0.03 mbar for 8 h, then soaked in Calgon (buffered sodium hexametaphosphate $[NaPO_3]_6$) for 24 h. Samples were then washed through a 63 μm sieve with de-ionized water to separate the fine fraction from the sand-sized fraction. The recovered sand-sized fraction was then covered in Calgon again and placed on a shaker table for 2 h. Samples were then washed over a 63 μm sieve with de-ionized water followed by methanol to evaporate remaining water and dried in an oven at 50°C.

Coarse fraction (%CF) data were obtained during processing of the samples by weighing the dried bulk sediment ($bulk_w$) after freeze drying and prior to soaking with Calgon. The >63 μm fraction (coarse fraction) was then weighed once dried (CF_w). The %CF was then calculated using the following formula:

$$\%CF = \left(CFw \div bulk_w\right) \times 100 \quad (1)$$

The >63 μm CF in this core is made up almost entirely of foraminifera. CF percent abundance is therefore affected by foraminiferal productivity and/or preservation.

3.1.1. Foraminifera

Specimens of the planktic foraminifera species *Dentoglobigerina venezuelana* and the benthic genus *Cibicidoides* were picked from the 250–400 μm fraction for geochemical analysis. Where abundance allowed, only the species *Cibicidoides mundulus* was used for stable isotope analyses; a total of 16 samples (out of 162) used other *Cibicidoides* species in the analyses. Of these 16, nine were monospecific analyses of other *Cibicidoides* species and seven were mixtures of other *Cibicidoides* with *C. mundulus*. Planktic foraminiferal species-specific stable isotope and trace element analyses were conducted on the species *D. venezuelana*, a species that is abundant throughout the Oligocene-Miocene (Wade et al., 2018) and has been previously used for geochemical analyses for this time interval (e.g., Stewart et al., 2012, 2017; Wade & Pälike, 2004).

3.1.2. Calcareous Nannofossils

A total of 51 samples were studied for the presence/absence of calcareous nannofossil marker species under a cross-polarised light microscope with a rotating stage at 1,000x magnification in order to provide a robust biostratigraphic framework for the core, to supplement existing lower resolution data from Flores et al. (2014). Smear slides were prepared using standard techniques (Bown & Young, 1998). Identified calcareous nannofossil bioevents are reported in the Table S1 along with the bioevents used to construct the age model (Table S2). Ages are calibrated to the timescale of Gradstein et al. (2012).

3.2. Foraminiferal Stable Isotope Analysis

Paired planktic and benthic foraminiferal stable carbon and oxygen isotopes ($\delta^{13}C$ and $\delta^{18}O$) were analyzed for insights into surface and bottom water oceanography. A total of 166 multi-specimen samples were analyzed between the depths 233.99–280.11 mbsf. $\delta^{13}C$ and $\delta^{18}O$ data were generated at the British Geological Survey using an IsoPrime 100 Gas Source Isotope Ratio Mass Spectrometer with Multiprep Device. Average analytical error (2σ) was 0.06‰ for $\delta^{13}C$ and 0.08‰ for $\delta^{18}O$ ($n = 25$) for the standard (KCM) analyzed at the same time. Data are reported relative to the Vienna Pee Dee Belemnite scale.

3.3. Planktic Foraminiferal Trace Element Analysis

Specimens of the planktic foraminifera *D. venezuelana* were also analyzed for trace elements, paired with stable isotope analyses, with the primary aim to derive planktic foraminiferal Mg/Ca temperatures (see

Section 3.3.1). Between 8 and 20 individuals were picked from each sample, then subsequently cracked, homogenised and split, with approximately 1/3 used for the stable isotopes and 2/3 for the trace element analyses. Samples with less than eight individuals were analyzed for stable isotopes only.

Trace element concentrations of 11 elements (Mg, Sr, Li, Ba, Cd, Nd, U, Mn, Fe, Al, Si) were analyzed on 87 of the split planktic foraminifera samples. Analyses were conducted at the Open University. Samples were cleaned using a modification of the method outlined in Boyle and Keigwin (1985). Samples were first washed in repeated Milli-Q and methanol rinses, ultrasonicating for ~10 s with each rinse, in order to remove any clays. Samples then underwent both a reducing step (ammonia solution and hydrous hydrazine) and an oxidative step (hydrogen peroxide [H_2O_2] and sodium hydroxide [NaOH]) in order to remove Fe-Mn coatings and organic material respectively (Pena et al., 2005). Finally, samples were polished using a weak (0.001 M) HNO_3 leach and subsequently dissolved in 0.075 M HNO_3.

Samples were analyzed using an Agilent Technologies Triple-Quadrupole Inductively Coupled Plasma Mass Spectrometer (QQQ-ICP-MS). An aliquot of sample solution was first used to check [Ca] prior to preparing samples at a fixed [Ca] of 10 ppm for trace element analysis to matrix match with synthetic standards (Rosenthal et al., 1999). Error in analyses were calculated based on a repeat measurement of a synthetic monitor standard during the analytical window (Mg/Ca of 3.32 mmol mol^{-1} with a 2σ of 0.19 mmol mol^{-1} and Mn/Ca of 146.46 μmol mol^{-1} with a 2σ of 5.27 μmol mol^{-1}; $n = 12$). Ratios of Al/Ca and Fe/Ca were monitored and compared with Mg/Ca ratios to assess the efficiency of the cleaning method and any potential contamination (Figure S1). The ratio of Mn/Ca was used as a proxy for relative oxygenation at the site (Dickens & Owen, 1994).

3.3.1. Converting Mg/Ca to Temperature

The incorporation of Mg into foraminiferal test calcite is dependent on temperature; the higher the temperature, the greater the ratio of Mg to Ca (Elderfield & Ganssen, 2000). Incorporation of Mg in foraminifera tests has also been shown to be sensitive to both changes in Mg/Ca of seawater (Mg/Ca_{sw}) and pH (Evans, Wade, et al., 2016; Gray & Evans, 2019) in various species. To assess the potential impact of Mg/Ca_{sw} and pH, measured planktic Mg/Ca values were corrected using Oligo-Miocene modeled pH values (Zeebe & Tyrrell, 2019) and using the linear regression equation (Equation 2) from Evans, Wade, et al. (2016). The average pH value used was 8.004 ± ~0.2. Mg/Ca-temperature was also calculated using a 3-Myr moving average of pH values which acted to lower temperatures by approximately 1ºC; this was smaller than the calculated error, and was therefore not implemented for these analyses.

$$\frac{Mg}{Ca} = -0.70 \times pH + 6.7 \tag{2}$$

D. venezuelana is extinct, so no species-specific calibration exists. Thus, temperature (T in °C) was calculated using the multi-species calibration of Anand et al. (2003) (Equation 3) with adjustments of the exponential and pre-exponential constants as per Evans, Brierley, et al. (2016) (Equations 4 and 5):

$$\frac{Mg}{Ca} = B\exp^{AT} \tag{3}$$

where

$$A = -0.0029 \times \frac{Mg}{Ca_{sw}^2} + 0.032 \times \frac{Mg}{Ca_{sw}} \tag{4}$$

$$B = 0.019 \times \frac{Mg}{Ca_{sw}^2} - 0.16 \times \frac{Mg}{Ca_{sw}} + 0.804 \tag{5}$$

An estimate for Oligocene Mg/Ca_{sw} of 2.15 mol mol^{-1} was taken from Evans et al. (2018) and assumed to be constant throughout the investigated interval as high-resolution data of Mg/Ca_{sw} for this time interval is not available. Mg/Ca_{sw} values from Horita et al. (2002) form an error envelope on the pre-exponential and exponential constants (maximum Mg/Ca_{sw} value of 2.92 mol mol^{-1} and minimum value of 1.67 mol mol^{-1}) due to the uncertainties in the Mg/Ca_{sw} estimations through this interval. The differences between the three calibrations (i.e., Anand et al., 2003 and Evans, Brierley et al., 2016 with and without pH adjustment) are shown in Figure S2; the trends remain the same throughout, but with differences in absolute temperatures. The average temperature from the three calibrations is presented in subsequent figures. Calculation of the

error propagation of Mg/Ca-temperature estimates is shown in the Supporting Information S1, with the calculated propagated error being 2.93°C.

3.3.2. Calculating Upper Water Column $\delta^{18}O$ ($\delta^{18}O_{sw}$)

The geochemical assessment of various size fractions of *D. venezuelana* suggests that it did not host photosymbionts during its life cycle (Stewart et al., 2012). As such, when calculating $\delta^{18}O_{sw}$ it is appropriate to use the low light calibration from Bemis et al. (1998) to most accurately reflect the relationship between $\delta^{18}O_{sw}$ and foraminiferal test chemistry (Equation 6).

$$T\left(\text{°C}\right) = 16.5 \pm 0.2 - 4.8 \pm 0.16 \times \left(\delta^{18}O_c - \delta^{18}O_{sw}\right) \quad (6)$$

This calculation was performed using the various options for temperature reconstructions described above (Figure S2). The average $\delta^{18}O_{sw}$ from the three calibrations is used in Figure 6. Error propagation calculations for the $\delta^{18}O_{sw}$ estimates are shown in the Supporting Information S1, with the calculated propagated error being 1.79‰.

3.4. Core Scanning X-Ray Fluorescence (XRF)

Core scanning XRF was undertaken at Woods Hole Oceanographic Institution using a Cox Analytical ITRAX with a Mo X-Ray tube set to 60 kV and 30 mA with a 15 s count time. The XRF spectra were interpreted, and the peak areas were quantified using software Q-Spec. A suite of 13 elements were analyzed at 4 mm resolution. Raw counts of Ca are calibrated against values of $CaCO_3$ wt% (this study; see below and Figure S3), thus absolute counts detected in XRF have been used quantitatively. Other elements were not calibrated against absolute concentrations of the same sediment samples, therefore only ratios of XRF elemental count data are used. Core scanning XRF-derived elemental ratio of Ti/Ca was used as a proxy for terrigenous input versus biogenic carbonate, Mn/Ti and Mn/Fe were used as proxies for redox conditions (see Rothwell & Croudace, 2015 and references therein).

3.5. Inductively Coupled Plasma Optical Emission Spectroscopy (ICP-OES)

A total of 46 bulk samples were analyzed on an ICP-OES Agilent 5110 Series at the University of Exeter Penryn Campus at a resolution of ~1 m. Bulk samples were micro-drilled and weighed at 500–1000 μg using an MSE3.6P-000-DM Sartorius Cubis Micro Balance. The samples were dissolved using 2% HNO_3 and diluted to a nominal Ca concentration of 25 μg g^{-1}. Solutions were run with the limestone standard JLs-1 and synthetic quality control solutions BCQC in order to assess data quality. Ca concentration data were used to calculate percentage calcium carbonate ($CaCO_3$ wt%) by comparing the theoretical amount of Ca present in the samples based on their weight, versus the measured Ca values in each sample (e.g., Razmjooei et al., 2020). The error, based on the reproducibility of the JLs-1 standard, was measured at 0.6% (2 rsd; $n = 12$), plus the associated weighing error (estimated at ~1%) giving a combined error of 1.2% for $CaCO_3$ wt%.

3.6. Scanning Electron Microscope (SEM)

A scanning electron microscope was used to image representative specimens of *Dentoglobigerina venezuelana* and *Cibicidoides* cf. *mundulus* (Figure 3) in order to assess preservation. Samples were imaged from intervals of both high and low percentage coarse fraction, which in other sites has been related to variable carbonate preservation (e.g., Littler et al., 2014). Analysis was carried out at the University of Exeter, Penryn Campus on a TESCAN VEGA3 GMU SEM. Samples were carbon coated prior to analysis and examined at 20 kV, at a working distance of 2.55–11.88 mm. Images were taken in both back scattered election and secondary electron modes.

3.7. Terrigenous Flux

The rate of terrigenous mass accumulation (MAR) can be used to reveal insights into non-carbonate related sedimentation at a site, assuming minimum contribution from biogenic silica. The terrigenous MAR was calculated using high-resolution $CaCO_3$ (wt%), dry bulk density (DBD), and linear sedimentation rate (LSR) as follows:

$$MAR = \left[\left(100 - CaCO_3\right) \times \text{DBD} \times \text{LSR}\right] \div 100 \quad (7)$$

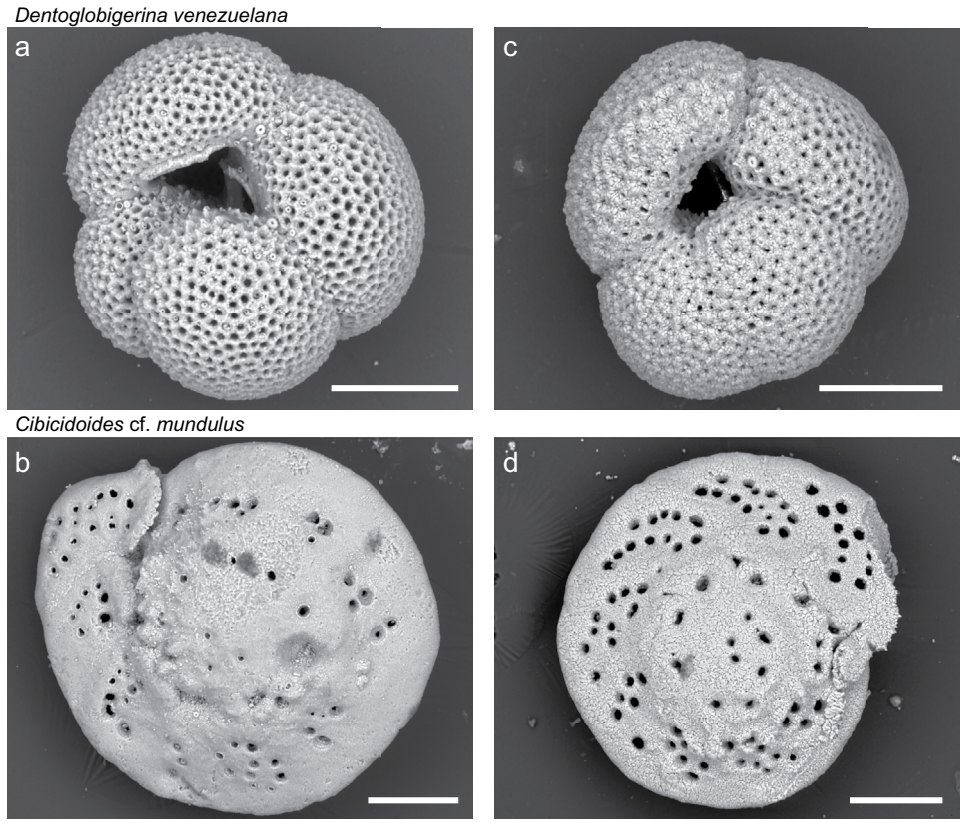

Figure 3. Scanning Electron Microscope images of foraminiferal species *D. venezuelana* (planktic) and *C* cf. *mundulus* (benthic) used in stable isotope and trace element analyses. Specimens a (24.4 Ma) and b (21.1 Ma) from intervals with high (5%–8%) percentage coarse fraction and high (70%–80%) $CaCO_3$ wt%. Specimens c (~22.4 Ma) and d (~22.5 Ma) from intervals with low (~0.5%) percentage coarse fraction and lower (~50%–60%) $CaCO_3$ wt%. Note more optimal preservation (clear pores and minimal dissolution) in specimens from higher percentage coarse fraction intervals (a) and (b). Scale bars are 100 μm.

High-resolution $CaCO_3$ (wt%) was calculated (Figure S4; $R^2 = 0.9558$) using Ca counts from core-scanning XRF calibrated to discrete sample measurements of $CaCO_3$ (wt%) performed at WHOI using JY Ultima C ICP-OES following methodology from Bertrand et al. (2012); (based on Murray et al., 2000). High-resolution DBD was calculated using discrete sample measurements of DBD correlated to high-resolution multi-sensor core logging density measurements from shipboard data (Figure S4; $R^2 = 0.4851$). The LSR from the biostratigraphic age model were also used.

4. Results

4.1. Age Model

Calcareous nannofossil datums originally identified in Flores et al. (2014) at a relatively low resolution were constrained further in this study to decrease the depth uncertainty associated with each event (blue circles; Figure 4). Two bioevents were not further constrained due to large age uncertainties (orange circles; Figure 4). Sedimentation rates calculated between each age control point (Figure 4) were then used to build an age model by assuming linear sedimentation rates between points. Due to the low resolution of benthic stable isotope data, it was not possible to astronomically tune the record for the age model, and shipboard magnetostratigraphy was not conducted. Despite this, our biostratigraphic age model appears robust, and is particularly well-constrained around the Oligocene-Miocene boundary. Benthic stable isotope trends are consistent with high-resolution records, which provides support for the implemented age model (Figure 5).

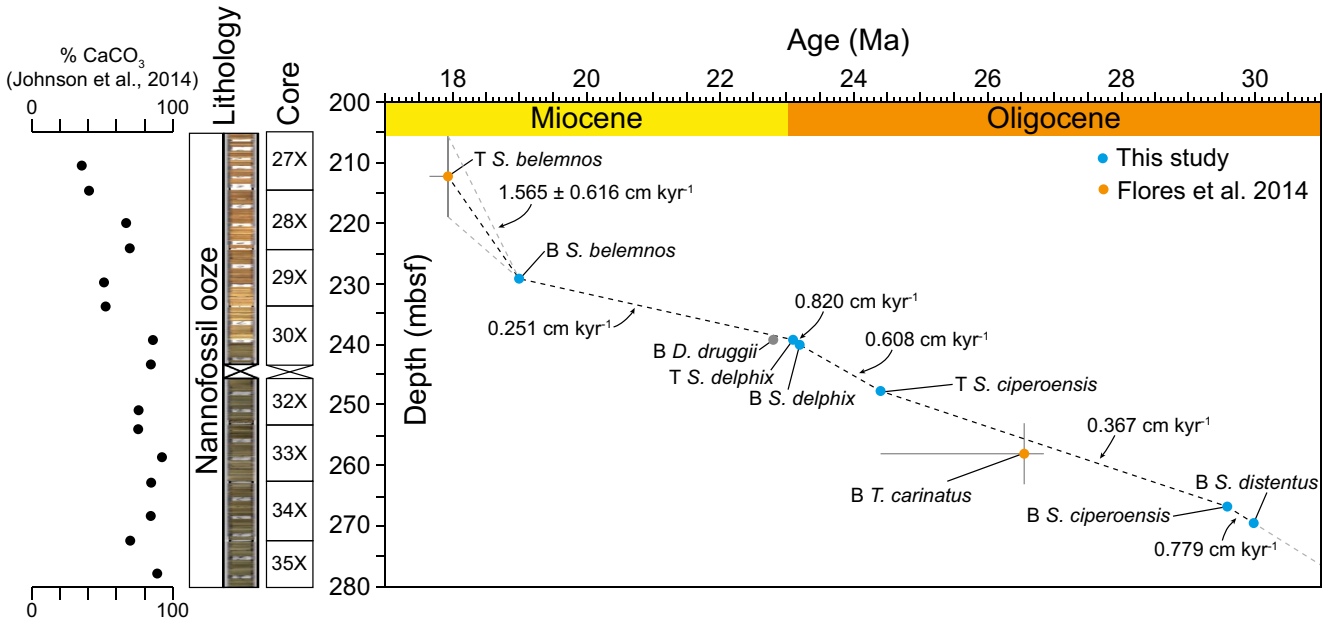

Figure 4. Age-depth plot constructed using the calcareous nannofossil events listed in Tables S1 and S2. B is base of biozone, T is top of biozone. Where no depth error can be seen, error is smaller than data point plotted. Dashed line shows linear interpolated sedimentation rate, with numbers showing calculated sedimentation rates between tie points (in cm kyr^{-1}) used to construct age model (Table S2). Core lithology and core images are shown on the left-hand side. White boxes in the core photos are missing core due to sampling for gas hydrates. Low resolution percentage calcium carbonate data from Johnson et al. (2014) shows decrease approximately coincident with change in core color ~240 mbsf. Gray data point (*Discoaster druggii* first occurrence) was not used to construct the age model due to poor age constraint on this bioevent, but its approximate position in time is plotted here as an additional qualitative constraint (Young, 1998). Orange data points were not further constrained from Flores et al. (2014) position due to associated age uncertainties: B *T. carinatus* ~26.84–24.40 Ma (Young, 1998) and T *S. belemnos* ~17.95–17.67 Ma (Bergen et al., 2017; Gradstein et al., 2012).

From 262–280 mbsf (lower/middle Oligocene) samples were taken at a resolution of ~50 cm, equating to an approximate temporal resolution of 65 kyr between samples. The sections 243–262 mbsf (late Oligocene) and 214–224 mbsf (early Miocene) were sampled at a ~15 cm resolution, an approximate temporal resolution of 10–40 kyr. The section 224–243 mbsf (Oligocene-Miocene boundary) was sampled at an ~8 cm resolution or a sample every ~13 kyr in the late Oligocene or ~30 kyr in the early Miocene.

4.2. Percentage Coarse Fraction (%CF) and Percentage Calcium Carbonate

The core is carbonate-rich throughout, with $CaCO_3$ wt% values varying between 45% and 90% (Figure 6a). The highest $CaCO_3$ wt% values are found in the latest Oligocene with distinctly lower values in the Miocene; this is also visible in the cores with an increased brown coloration up section suggesting higher relative clay content (Figure 4). The average percentage coarse fraction (%CF), which is related primarily to foraminiferal content, was 3.85% throughout the whole core, with a maximum value of 11.86% and a minimum of 0.23% (Figure 6c). Two sustained minima (~200 kyr long) of %CF were observed in the core at ~25 Ma (late Oligocene) and ~22.5 Ma (early Miocene). At the 25 Ma %CF minima, values of $CaCO_3$ wt% remain at ~70%–80%. At 22.5 Ma the minimum in %CF coincides with lower $CaCO_3$ wt% of 50%–60%. Within this interval of low %CF and low $CaCO_3$ wt% both benthic and planktic foraminifera were less well-preserved, as observed by SEM imaging (Figure 3). Despite this, there is no correlation between %CF and either oxygen isotope values or Mg/Ca-derived temperatures in the whole record (Figure S5), suggesting that these proxies have not been affected by diagenetic alteration in the core (Edgar et al., 2013). At 23 Ma $CaCO_3$ wt% decreases from ~80% to ~60%; values of $CaCO_3$ wt% remain around 60% until the end of the record at 20 Ma.

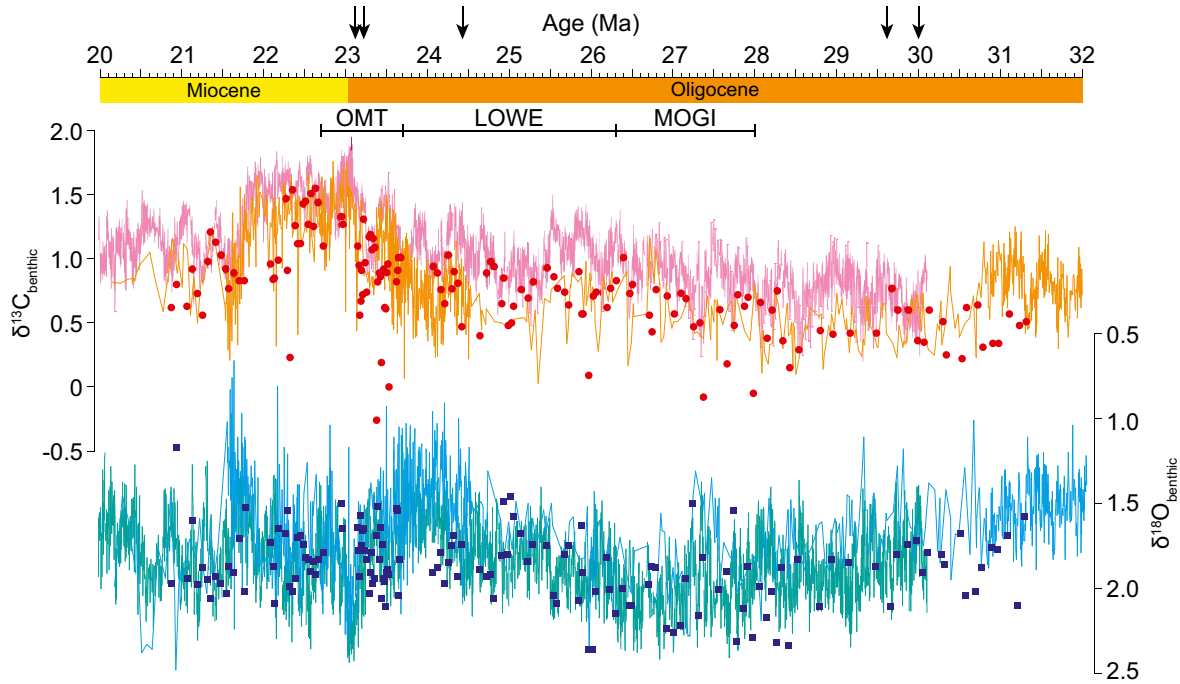

Figure 5. Benthic foraminiferal stable carbon (red circles) and oxygen (blue squares) isotope data from this study (Site NGHP-01-01A; paleodepth ~2,250 mbsl) on the new biostratigraphic age model (Figure 4) against other contemporaneous high-resolution data (raw carbon isotope data). ODP Site 1218 (Pälike et al., 2006; paleodepth ~4,200 mbsl) in the eastern equatorial Pacific in orange and light blue. ODP Site 1264 (Liebrand et al., 2016; paleodepth ~2,500 mbsl) in the equatorial Atlantic in pink and green. Carbon isotopes show good correlation between the records, with offsets in absolute values likely due to different ages of deep-water masses in each ocean basin. Oxygen isotopes show generally similar overall values between sites, with some differences in trends, for example, in the late Oligocene interval where data from the Arabian Sea (this study) remain more positive relative to the Pacific and Atlantic datasets.

4.3. Foraminiferal Stable Isotope Analysis

Benthic foraminiferal oxygen isotopes ($\delta^{18}O_b$) have an average value of ~+1.9‰ throughout the record (Figure 6d). In the middle Oligocene, from 31.5–27 Ma, $\delta^{18}O_b$ values increased by approximately 0.6‰ from ~+1.7‰ to ~+2.2‰. Subsequently, there is a decreasing trend (warming/ice loss) from ~+2.1‰ at 26 Ma to ~+1.6‰ at 25 Ma, the approximate time frame of the LOWE. At ~24.9 Ma there is a rapid 0.5‰ increase in $\delta^{18}O_b$ over 0.12 Myr, followed by a subsequent decrease of 0.3‰ over ~1.9 Myr. From 23.1 to ~22.6 Ma (latest Oligocene to early Miocene) $\delta^{18}O_b$ once again increased by ~0.3‰, with values then remaining more stable from 22.6 to 21 Ma at ~+1.7 to +2‰. Planktic foraminifera oxygen isotope ($\delta^{18}O_p$) values are −0.5 to +0.5‰ between ~31.5 and 23.5 Ma (middle to late Oligocene), with a number of spikes to more negative values of up to −2‰ (Figure 6e). From 23.5 Ma to 22 Ma (~OMT) $\delta^{18}O_p$ values have a decreasing trend from +0.5‰ to −1.0‰, with a positive spike within this trend at ~22.6 Ma. From 22 Ma $\delta^{18}O_p$ values once again become more positive, with values ranging from −1‰ to +0.1‰.

Benthic carbon isotopes ($\delta^{13}C_b$) show an overall increasing trend from ~28 Ma, from values of +0.5‰ to a maximum of +1.5‰ at ~22.5 Ma (Figure 6f). From 22 Ma values show a decrease of ~0.8‰. Prior to 28 Ma (middle Oligocene), planktic carbon isotopes ($\delta^{13}C_p$) are ~+1‰ (Figure 6g). From ~28 to 23 Ma (late Oligocene) $\delta^{13}C_p$ values show an overall 1‰ increase, with significant higher frequency variability on the order of ±1‰. After 23 Ma (early Miocene) $\delta^{13}C_p$ values stabilize at between +1‰ and +1.5‰ with variability <±1‰. Benthic carbon and benthic oxygen isotopes show generally similar trends to other equatorial sites in the Pacific and Atlantic through the Oligocene to Miocene interval (Figure 5). Prior to 27 Ma (late Oligocene) $\Delta\delta^{13}C$ (benthic minus planktic carbon isotopes) is −0.5‰; from 27 Ma values trend towards +0‰, with occasional intervals where planktic carbon isotopes are more negative than benthic carbon isotopes (i.e., $\Delta\delta^{13}C$ is positive). This is especially apparent from 23.5–22.3 Ma (latest Oligocene to earliest Miocene). Average $\Delta\delta^{13}C$ values for the investigated interval are −0.29‰, with benthic values being on average more negative than planktic values, as would be expected in normal open marine settings (Figure 6h).

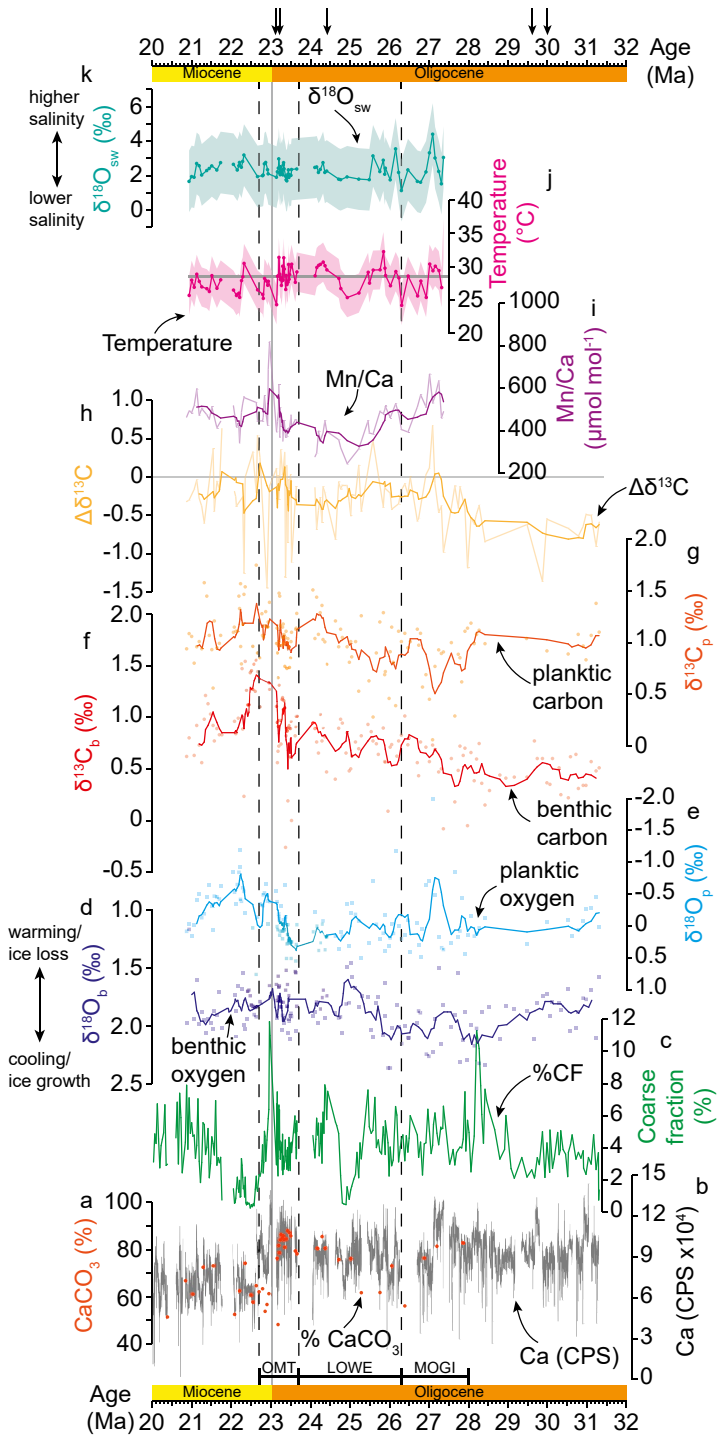

Figure 6. Geochemical and sedimentological analysis of bulk sediment and benthic and planktic foraminifera from Site NGHP-01-01A spanning the middle Oligocene to early Miocene (~31.5–20 Ma). Vertical dashed lines show boundaries between climate intervals of Liebrand et al. (2017); MOGI = mid Oligocene glacial interval; LOWE = late Oligocene warming event; OMT = Oligocene-Miocene transition. Vertical gray line depicts Oligocene-Miocene boundary (~23 Ma). Black arrows show biostratigraphic tie points used to construct age model (Table S1). (a) Weight percent $CaCO_3$ (orange circles); (b) XRF-derived Ca in CPS (gray line); (c) Percentage coarse fraction (%CF; green line); (d) Benthic ($\delta^{18}O_b$) and (e) Planktic ($\delta^{18}O_p$) foraminiferal oxygen isotopes (squares) with 5-point running averages (solid lines); (f) Benthic ($\delta^{13}C_b$) and (g) Planktic ($\delta^{13}C_p$) foraminiferal carbon isotopes (circles) with 5-point running averages (solid lines); (h) Calculated difference between planktic and benthic carbon isotope values ($\Delta\delta^{13}C$); (i) Planktic foraminiferal Mn/Ca (μmol mol^{-1}) with 5-point running average; (j) Temperature and (k) $\delta^{18}O_{sw}$ derived from thermocline dwelling planktic foraminifera *Dentoglobigerina venezuelana*. Modern mean annual sea surface temperature (~28.5°C) depicted by horizontal gray line (from Ocean Data View).

4.4. Planktic Foraminiferal Trace Element Analysis

We used Mg/Ca ratios to calculate an upper water column paleotemperature record (see Methods), and Al/Ca and Fe/Ca ratios to monitor for contamination by clays (Figure S1). Both Al/Ca and Fe/Ca show no correlation with Mg/Ca (R^2 values = 0.0084 for Al/Ca, 0.0365 for Fe/Ca), suggesting effective cleaning and a negligible effect of clays on Mg/Ca ratios. From ~27.5 Ma to 26 Ma Mg/Ca values remain around the overall average (3.33 mmol mol^{-1}). At 26 Ma and 24 Ma values peak at ~4 mmol mol^{-1}, with a low between these peaks of ~2.9 mmol mol^{-1}. From 24 Ma onwards Mg/Ca values show an overall decrease of ~1 mmol mol^{-1} from 4 to 3 mmol mol^{-1} over ~3 Myr. Between 21–22 Ma values remain steady at 3 mmol mol^{-1} (Figure S2).

The overall values of Mn/Ca were high at ~300–800 μmol mol^{-1} (2σ = 5.27 μmol mol^{-1}), however, there is no significant correlation (R^2 = <<0.1) between Mn/Ca or any of the other elemental ratios (Figure S6) suggesting that that Mn-rich phases have little overall effect on trace element compositions. A reductive step was included in the cleaning of foraminiferal samples prior to trace element analysis, which acts to remove diagenetic Fe-Mn crusts to ensure that only the primary Mn signature is measured. From 27.5–23.5 Ma the Mn/Ca ratio varies between ~400–600 μmol mol^{-1}. From ~23.5–22.9 Ma values peak at up to 800 μmol mol^{-1}, subsequently then decreasing to ~500 μmol mol^{-1} from 22.9–21 Ma.

4.4.1. Mg/Ca-Temperature Calibrations

The average temperature difference between the different Mg/Ca-temperature calibrations is ~7°C (Figure S2). The multi-species calibration from Anand et al. (2003) resulted in the lowest average temperatures (24°C) and the Evans, Brierley, et al. (2016) calibration without a pH correction produced the highest average temperatures (31°C). Despite these differences in absolute temperatures, overall trends are very similar (Figure S2). From 27.4 Ma to ~25 Ma (late Oligocene) there is ~5°C of overall temperature decrease, superimposed with higher resolution orbital-scale variability (Figure 6j). In the latest Oligocene at 25 Ma temperatures increase by approximately 4–7°C (calibration dependent) over ~0.6 Myr, after which they become more stable until 23.2 Ma where there is a rapid (~60 kyr; 23.20–23.14 Ma) temperature decline of 2°C–4°C. Two further cycles of gradual warming and rapid cooling then follow from ~23.1–22 Ma with temperature variability of ~5°C. From 22 Ma in the early Miocene values appear to stabilize at 25°C–30°C. Average values ~23.2–21 Ma are 1.2°C–2°C cooler than the preceding interval of ~27.5–23.2 Ma.

4.4.2. Upper Water Column $\delta^{18}O$ ($\delta^{18}O_{sw}$)

Calculated $\delta^{18}O_{sw}$ values vary by ~1‰–2‰ due to the different temperature calibrations used, however trends between the different calibrations are similar (Figure S2). In general, values from 27.5–25.5 Ma (late Oligocene) are highly variable, with maximum values of +5‰ and minimum values +1.5‰ (if using the Evans, Brierley, et al., 2016 calibration). From 25.5–21.0 Ma (late Oligocene to early Miocene) values are more stable, remaining at approximately +3 ± 0.5‰ during this interval (Figure 6k).

4.5. XRF Core Scanning

All XRF-derived elemental ratio records appear to show cyclicity coinciding with short eccentricity pacing (~100 kyr cycles; Figure 7) based on the new biostratigraphic age model, however, cyclostratigraphic analysis of the records was not possible as frequent core gaps were present due to gas hydrate sampling (Figure 4).

The ratio of Ti/Ca can be used to track the changing flux of terrestrially derived Ti against $CaCO_3$ through time. There is clear optical evidence that the $CaCO_3$ in these sediments is dominated by calcareous nannofossils and foraminifera (Collett et al., 2008; Flores et al., 2014; this study), suggesting a dominantly biogenic origin of the $CaCO_3$. The good correlation of XRF-derived Ca counts per second (CPS) against $CaCO_3$ wt% (R^2 = 0.58) and XRF-derived Ca/Ti against $CaCO_3$ wt% (R^2 = 0.70; Figure S3) suggests the XRF-derived CPS can be used as a proxy for changing $CaCO_3$ content in the core (Figure 6a). There is a clear step-change in Ti/Ca ratio at ~23.2 Ma, just prior to the Oligocene-Miocene boundary, where baseline Ti/Ca increases by ~95% (~0.01 CPS) relative to the Oligocene. Prior to this step increase there are higher-frequency changes in Ti/Ca that appear to occur on ~100 kyr eccentricity timescales (Figure 7).

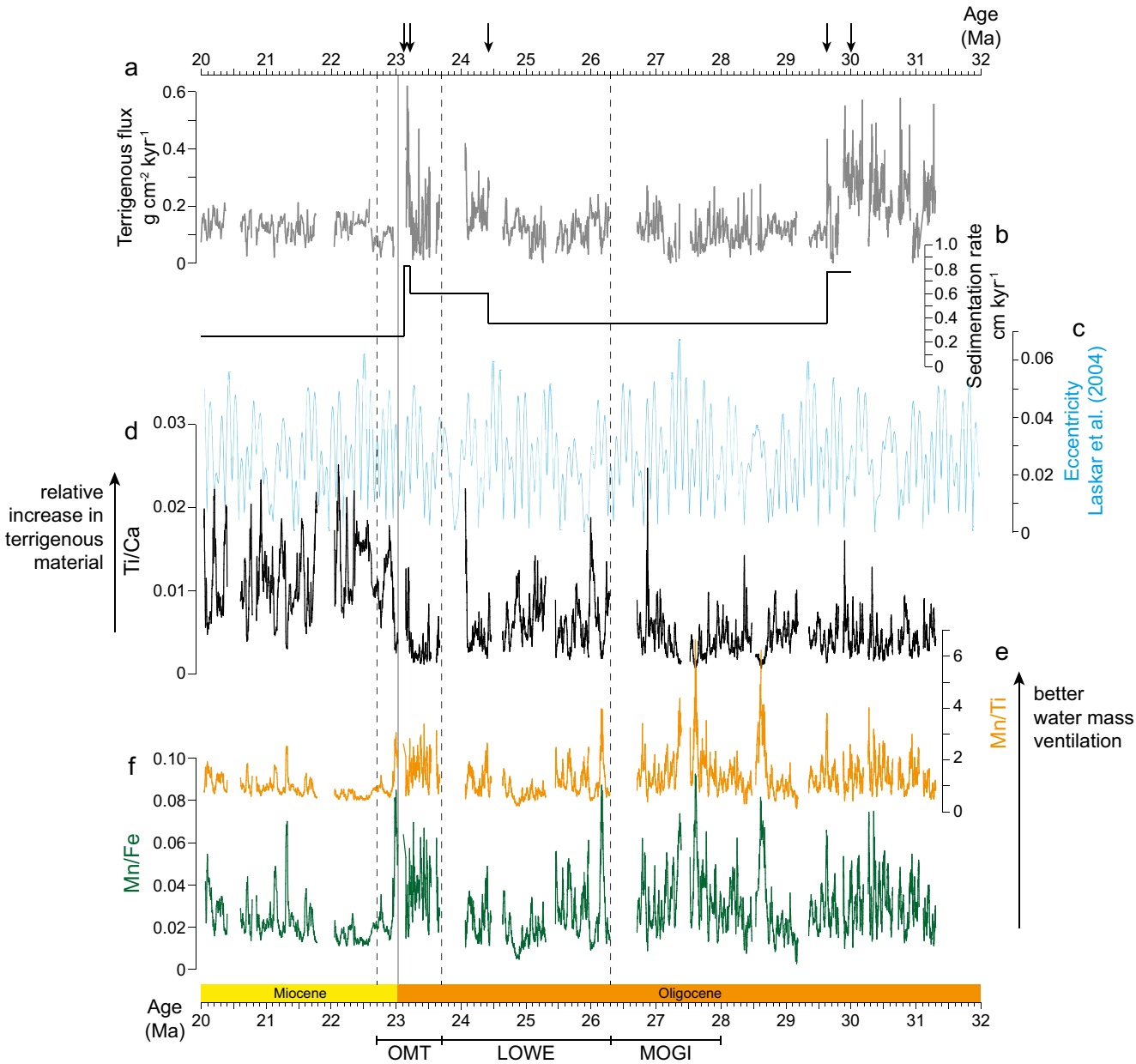

Figure 7. (a) Terrigenous flux (g cm^{-2} kyr^{-1}). (b) Sedimentation rate (cm kyr^{-1}). (c) Laskar et al. (2004) eccentricity solution. Core-scanning XRF-derived elemental ratios (5-point running averages) of Ti/Ca (d), Mn/Ti (e), and Mn/Fe (f). Gray line depicts Oligocene-Miocene boundary. Dashed lines depict boundaries between OMT, late Oligocene warming event and MOGI (Liebrand et al., 2017), abbreviations as in Figure 6. The gaps in the data are due to gas hydrate sampling during the coring expedition; the gap around 26.5 Ma was due to difficulties running core scanning XRF analysis on one section, thus this is not a gap in other data sets.

Raw XRF-derived Ti counts (CPS) increase by 88% at 23.0 Ma. Raw XRF-derived Ca CPS also show a step-decrease; however, this occurs at ~22.7 Ma (early Miocene). This change also appears to be stratigraphically offset from the decrease in $CaCO_3$ wt% that occurs in the early Miocene at ~23.0 Ma, suggesting that some of the Ca detected in the core scanning XRF data could be derived from clay minerals, rather than exclusively from biogenic $CaCO_3$ (Figure 6a).

Mn/Ti and Mn/Fe also show clear orbital-scale variability throughout the Oligocene interval, with a switch to lower baseline ratios at the Oligocene-Miocene boundary (Figure 7). Prior to this decrease, there is a short interval through the OMT (~23.6–22.9 Ma) where values remain at a higher baseline, with no obvious imprint of short eccentricity as is seen throughout the late Oligocene.

4.6. Terrigenous Flux

In general, the terrigenous flux (Figure 7a) reflects the sedimentation rate (Figure 7b). Values vary from ~0.1–0.3 g cm^{-2} kyr^{-1} from 30.0–23 Ma, with a very minor reduction in variability to 0.1–0.2 g cm^{-2} kyr^{-1} from 23–20 Ma. Values 30–31.5 Ma are higher than the average for the record, at ~0.3–0.5 g cm^{-2} kyr^{-1}; however, this may be driven by the uncertainty in the age model prior to 30 Ma, and subsequently the LSR, due to a lack of biostratigraphic tie points before 30 Ma.

5. Discussion

5.1. Change in *Dentoglobigerina venezuelana* Depth Habitat

Before drawing broad conclusions about surface water mass changes over time in terms of temperature, salinity, etc., derived from planktic foraminiferal archives, it is important to constrain any changes in the ecological niche that the target organism may have inhabited. Multi-species stable isotope analyses reveal that the planktic foraminifera species *Dentoglobigerina venezuelana* changed its depth habitat during the late Oligocene, from being a mixed layer dweller (Wade et al., 2007) to a thermocline dweller (Matsui et al., 2016; Stewart et al., 2012). The timing for this change is poorly constrained and appears diachronous across ocean basins, occurring as a two-step change in the eastern equatorial Pacific from 27.4–26.3 Ma (late Oligocene) at IODP Site U1334 (Matsui et al., 2016) and ODP Site 1218 (Wade & Pälike, 2004) and from 24 Ma (latest Oligocene) in the equatorial Atlantic (ODP Site 925; Stewart et al., 2012).

The difference between planktic and benthic carbon isotopes ($\Delta\delta^{13}C$: benthic minus planktic carbon isotopes) can provide insights into the depth habitat of a particular foraminifera species. At Site NGHP-01-01A in the Arabian Sea, at ~27 Ma there is a step shift in $\Delta\delta^{13}C$ towards values approaching 0‰ (Figure 6h) with almost no gradient for the remainder of the record. This convergence of benthic and planktic $\delta^{13}C$ values between ~28–27 Ma in the Arabian Sea, driven by planktic $\delta^{13}C$ becoming ~0.5‰ more negative, is consistent with the migration of *D. venezuelana* to a deeper, thermocline habitat. Other factors that could influence the carbon isotope gradient are a change in surface water primary productivity, or possibly an increase in water mass mixing. There is no concurrent change in other proxies to suggest a change in productivity, for example in the Ca in the core or the percentage coarse fraction (%CF; Figures 6b and 6c). There is also no concurrent change in proxies for water mass oxygenation (Mn/Fe or Mn/Ti ratios), which may be expected if the water mass became less stratified through increased mixing (Figure 7). We therefore favor the interpretation that the change in $\Delta\delta^{13}C$ at 27 Ma is a result of a deepening in *D. venezuelana* depth habitat to the thermocline, consistent with timing seen in the Pacific Ocean (Matsui et al., 2016; Wade & Pälike, 2004).

There is no concurrent step-change in $\delta^{18}O_p$ data at 27 Ma, merely a long-term increase in values of ~1‰ between ~30.5–23.5 Ma, suggesting this apparent change in depth habitat is not the primary driver of the trend in this parameter. Importantly, the Mg/Ca-derived temperature estimates for this record only begin at 27 Ma, by which time the $\Delta\delta^{13}C$ data suggest the depth migration of *D. venezuelana* in the Arabian Sea is complete: hence any subsequent variability in temperature or calculated $\delta^{18}O_{sw}$ across the late Oligocene to early Miocene is independent of additional depth migration issues and can be regarded as representing thermocline conditions.

5.2. Oligocene-Miocene Upper Water Column Temperature Evolution

The Mg/Ca-derived thermocline temperature recorded at Site NGHP-01-01A is characterized by relatively high variability for a tropical site, which is especially apparent over the period of the LOWE ~26.5–24 Ma; dark green squares in Figure 8. The reconstructed absolute temperatures and trends are broadly in line with other equatorial sites, especially those from equatorial Atlantic ODP Site 926 (light green squares; Stewart et al., 2017), also based on *D. venezuelana* Mg/Ca ratios. All things being equal, the TEX_{86}-derived temperatures would be expected to be warmer than the contemporaneous Arabian Sea temperatures as TEX_{86} is thought to track SST rather than thermocline temperatures; this may explain some of the cooler temperatures in the late Oligocene Arabian Sea data compared to the contemporaneous Atlantic data. In general, there is a ~2°C–4°C temperature decline over the OMT at all sites apart from ODP Site 929 in the equatorial Atlantic (dark gray circles; O'Brien et al., 2020). Temperatures recorded in the latest Oligocene and early

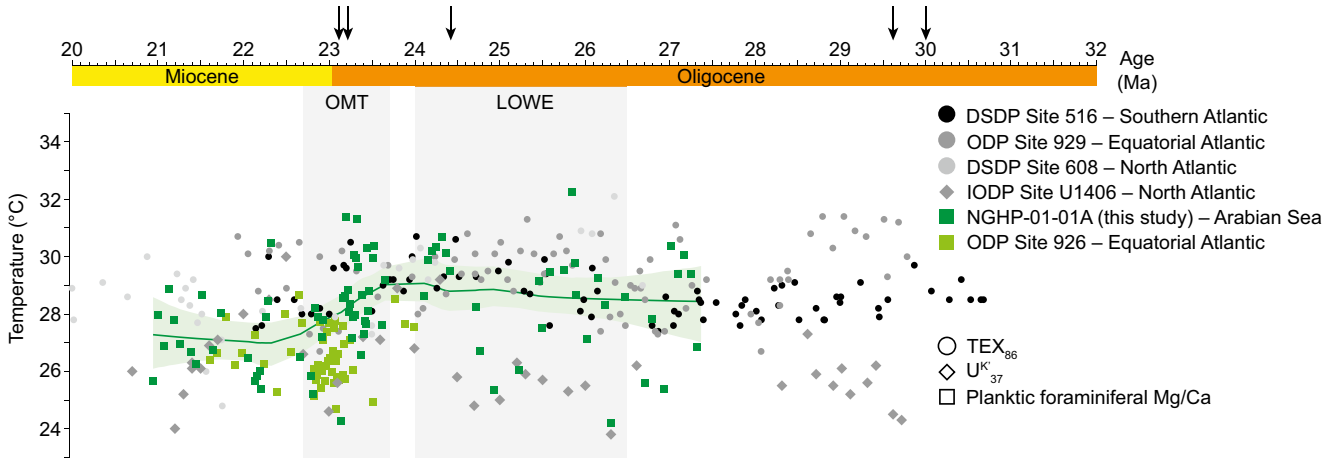

Figure 8. Site NGHP-01-01A (Arabian Sea) compared with other records of upper water column temperature. Planktic foraminiferal (*D. venezuelana*) Mg/Ca records are squares, data from Stewart et al. (2017; ODP Site 926) and this study. TEX_{86} records are circles, data from Super et al. (2018; DSDP Site 608) and O'Brien et al. (2020; ODP Site 929 and DSDP Site 516). $U^{K'}_{37}$ record in diamonds from Guitián et al. (2019; IODP Site U1406). Green data points are those recording thermocline temperatures, gray data points are those recording the surface/mixed layer. The green line is a LOESS curve (smooth = 0.4) and bootstrap confidence interval (shading) of the Arabian Sea data (this study). Arrows show biostratigraphic age model tie points for Site NGHP-01-01A record.

Miocene are generally very similar in all the records (~26°C–30°C), with somewhat higher variability in the range of temperatures in the early-middle Oligocene (temperatures ~25°C–31°C).

5.3. The Early Phase of the Oligocene-Miocene Transition (23.7–23.0 Ma)

The OMT encompasses a transient glaciation event (~23.7–23.0 Ma), followed by a deglaciation (recovery phase) into the early Miocene (~23.0–22.7 Ma; Liebrand et al., 2017). This event stands out from the background orbitally driven variability due to the magnitude of the excursion and the two-pulse structure of the positive $\delta^{18}O$ excursion, similar to the Eocene-Oligocene glaciation (~34 Ma; Coxall et al., 2005). It also terminates the long-term warming trend of the LOWE (Liebrand et al., 2017).

From the beginning of the OMT (~23.7 Ma; Liebrand et al., 2017) at Site NGHP-01-01A there is a decrease in the surface-to-deep carbon isotope gradient (decreased $\Delta\delta^{13}C$), an increase in XRF-derived sedimentary Mn/Ti and Mn/Fe ratios, and generally high $CaCO_3$ wt% contents (Figure 9). There is also an increase in foraminiferal Mn/Ca values beginning at ~23.3 Ma (Figure 6i). As it seems likely that *D. venezuelana* has completed its depth migration in this region by this point, the decrease in $\Delta\delta^{13}C$ at the start of the OMT is suggestive of either a decrease in surface water productivity and subsequent decrease in export productivity to deep waters, an increase in vertical water mass mixing stimulating carbonate productivity, or an incursion of a southern sourced (older) water mass with higher oxygen and carbonate ion content. The concurrent increase in Mn in the core (first bulk, then foraminiferal) suggests increased oxygenation during the early part of the OMT (23.7–23.0 Ma). Increased presence of Mn is generally thought to signal increased ventilation due to Mn becoming less soluble in a more oxygenated water mass (Barras et al., 2018). Importantly, in this study foraminiferal test calcite was cleaned using a reductive cleaning step in order to remove diagenetic Fe-Mn crusts prior to trace element analysis, and so this signal is not related to secondary contamination. While it is possible that some diagenetic crusts persisted after cleaning, there is no correlation between Mn/Ca ratios or any other trace element including Fe/Ca ($R^2 = <<0.1$; Figure S6). In the equatorial Atlantic *D. venezuelana* Mn/Ca ratios were also high (500–1,000 μmol mol^{-1}; Stewart et al., 2017), comparable to the values seen in the Arabian Sea. It is thought that Mn can be adsorbed onto foraminiferal test calcite within the water column, during sinking and prior to deposition (Davis & Benitez-Nelson, 2020) with Mn incorporation varying between species (Barras et al., 2018). A decline in Mn abundance in sediments has been used as a proxy for reduced oxygenation and oxygen minimum zone (OMZ) development in the northern Indian Ocean during the Miocene and Pliocene (Bialik et al., 2020; Dickens & Owen, 1994). All of these factors taken together suggest that during the early part of the OMT, until the Oligocene-Miocene

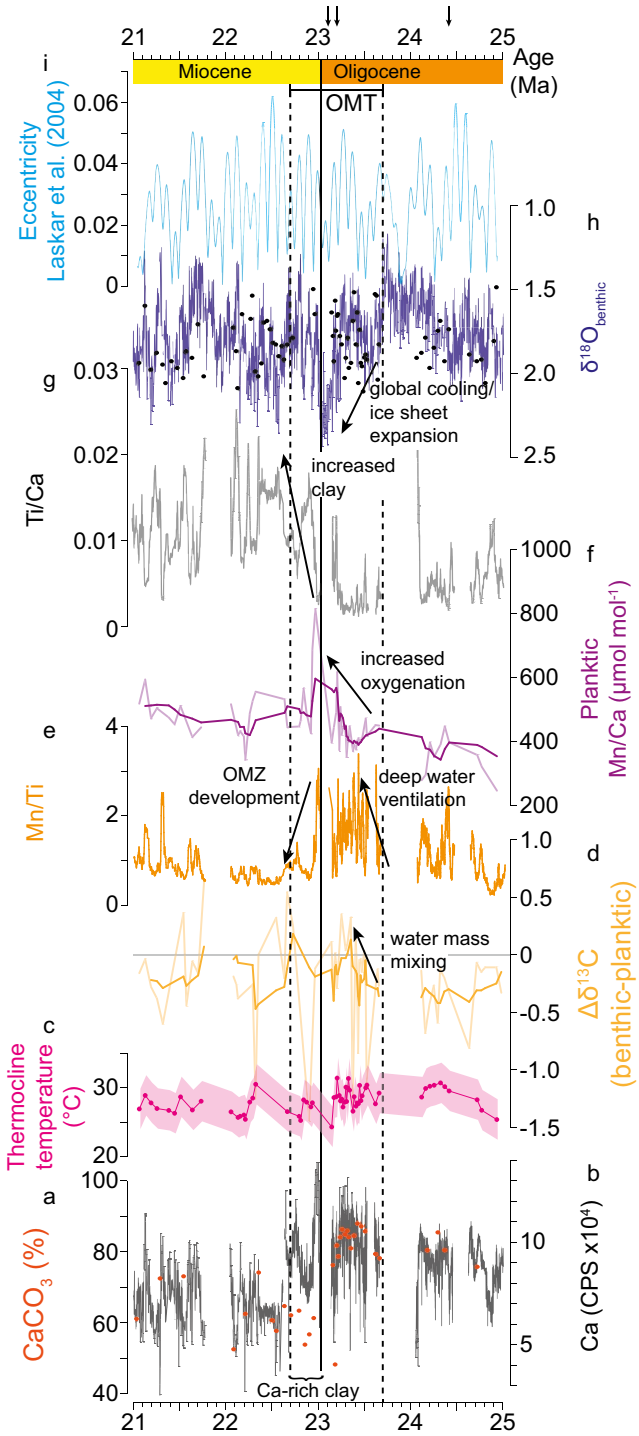

Figure 9. Geochemical data from NGHP-01-01A covering the late Oligocene to early Miocene (25–21 Ma). (a) CaCO3 wt% (circles); (b) XRF-derived Ca abundance (black line); (c) Planktic foraminiferal (thermocline) Mg/Ca-temperature; (d) Surface to deep carbon isotope gradient ($\Delta\delta^{13}C$); (e) XRF-derived Mn/Ti; (f) Planktic foraminiferal Mn/Ca with 5-point running average; (g) XRF-derived Ti/Ca ratio; (h) Benthic oxygen isotopes ($\delta^{18}O_b$) from ODP Site 1264 in the equatorial Atlantic (blue line; Liebrand et al., 2016) and Site NGHP-01-01A (black circles; this study); (i) Eccentricity solution from Laskar et al. (2004).

boundary (~23.7–23.0 Ma), there was increased ventilation of thermocline/intermediate waters at Site NGHP-01-01A resulting in high productivity, improved preservation (high $CaCO_3$ wt%, high %CF), and increased Mn incorporation.

This first part of the OMT (23.7–23.0 Ma) is associated with a global increase in benthic $\delta^{18}O$, thought to be due to the expansion of ice sheets in East Antarctica (Zachos et al., 1997, 2001), possibly driven by an extended period of low-amplitude orbital cyclicity (Figure 9i; Liebrand et al., 2011; Zachos et al., 2001). During past global cooling events (Bischoff & Schneider, 2014), Northern Hemisphere cooling (Broccoli et al., 2006), and changes in polar ice cover (Schneider et al., 2014), the intertropical convergence zone (ITCZ) has been shown to have moved equatorwards, possibly in response to increased net energy input at the low latitudes. With a relative southward shift of the ITCZ over the NGHP-01-01A study site, there would likely be stronger and dominant "winter monsoon" type atmospheric circulation (Dimri et al., 2016; Parvathi et al., 2017), that is, dry winds would dominantly flow from the Indian landmass in the northeast towards the Indian Ocean (SAWM; Figure 2b).

An average southward shift of the ITCZ during the Oligocene to Miocene glaciation has also been suggested to occur on the basis of data from the equatorial Pacific and Atlantic Oceans: a transient change in surface water flow direction is thought to have allowed the migration of planktic foraminifera *Paragloborotalia kugleri* from the Pacific into the Atlantic via the Central American Seaway (Fraass et al., 2019), and a temporary alteration in wind direction drove dust provenance changes in the equatorial Pacific (Hyeong et al., 2014). Due to the low-resolution nature of both of these datasets, exact timings for these changes are not well-constrained, however both are associated with the early OMT glaciation event ("Mi-1" event; Miller et al., 1991). Hyeong et al. (2014) propose the southward shift of the ITCZ may have been caused by an increased Northern Hemisphere cooling rate. This is supported by low-resolution TEX_{86}-derived SST datasets compiled from the Atlantic during the early phase of the OMT (Figure 10); these show a relatively warmer South Atlantic in comparison to the North Atlantic (Guitián et al., 2019; O'Brien et al., 2020; Super et al., 2018) providing a possible mechanism for the southward ITCZ shift.

With a southward shift of the ITCZ causing winter monsoon-like circulation in the Arabian Sea, surface water flows would be predominantly from the south to the north, along the western Indian continental margin (Figure 2b) (Lee, Jo et al., 2020, Lee, Kim et al., 2020). This would bring relatively warmer, southern sourced surface/thermocline waters to this site during the early OMT (~23.7–23.0 Ma). Relatively warmer thermocline temperatures are observed in the core over this glaciation interval (Figure 9c), possibly driven by such a change in the source of surface/thermocline waters.

5.3.1. Tectonic Changes Over the Oligocene to Early Miocene

Throughout the Paleogene and early Neogene, Tethyan Indian saline water (TISW) flowed from the Tethys into the northern Indian Ocean as a deep, saline water mass (Wright et al., 1992). This throughflow was dependent on the eastern Tethys gateway between Africa and Eurasia remaining deep and open (Figure 2a). The gateway gradually shallowed

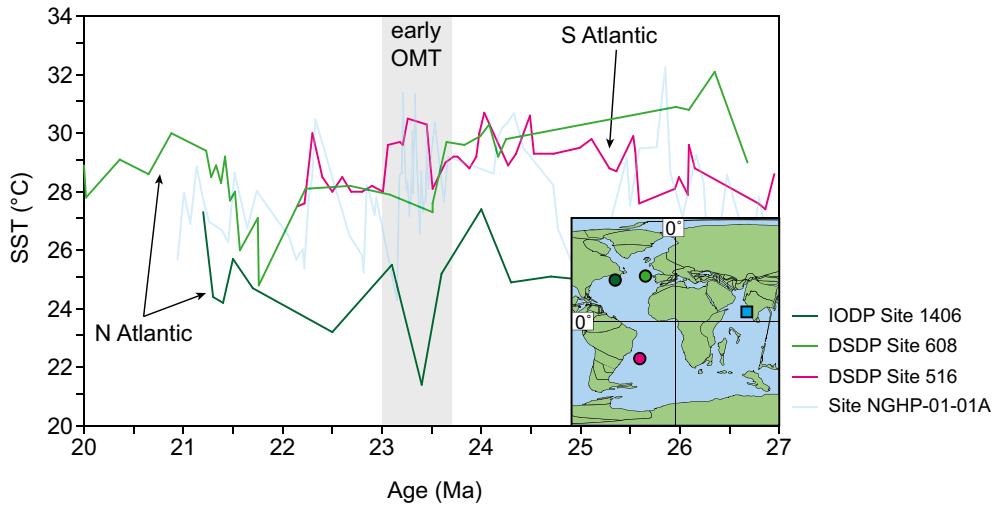

Figure 10. TEX_{86}-derived sea surface temperature records from the North Atlantic (green; IODP Site 1406 – Guitián et al., 2019; DSDP Site 608 – Super et al., 2018) and South Atlantic (pink; DSDP Site 516 – O'Brien et al., 2020). Also shown is planktic foraminiferal Mg/Ca-derived thermocline temperature from the Arabian Sea (light blue; Site NGHP-01-01A – this study). Gray box depicts the early phase of the Oligocene-Miocene transition (OMT; ~23.7–23.0 Ma). Note the relatively cooler North Atlantic and relatively warmer South Atlantic during the early OMT, providing a possible mechanism for the southward shift of the ITCZ during this interval. Inset map shows 23 Ma paleogeography and location of sites discussed.

from the late Eocene until its eventual closure in the middle Miocene (~14 Ma; Hamon et al., 2013). Modeling studies suggest that even with the gateway being ~250 m deep, effective TISW throughflow may have been compromised (de la Vara et al., 2013; Hamon et al., 2013). Global sea level fall over the OMT is thought to have been on the order of 50–65 m (Beddow et al., 2016; Miller et al., 2020; Wade & Pälike, 2004). As such, as the eastern Tethys gateway continued to shallow, reductions in relative sea level, for example transiently through a glaciation event, may have acted to temporarily change ocean circulation patterns in the Arabian Sea. If the intermediate TISW mass was temporarily restricted, this could have allowed a northward incursion of the intermediate Antarctic Intermediate Water and Subantarctic Mode Water (AAIW-SAMW), transiently affecting ocean circulation and thus foraminiferal geochemistry at Site NGHP-01-01A over the Oligocene-Miocene glaciation. However, at this time more evidence is required to support this hypothesis.

The role of changing tectonics/topography in the initiation of the Indo-Asian monsoon systems has been investigated through increasingly detailed modeling (Acosta & Huber, 2020; Chakraborty et al., 2009; Wei & Bordoni, 2016). Acosta and Huber (2020) show that monsoonal atmospheric circulation is established over the Bay of Bengal and Arabian Sea regions with sufficient SST gradients and subsequent seasonal movement of the ITCZ; however, the flow of moisture onto the continent and summer precipitation above 30°N is weak or absent without topographically forced (e.g., Himalayan-Tibetan Plateau-related) orographic precipitation. For Site NGHP-01-01A, direct precipitation in the models occurs over the locality even in the flat topographic simulation (Acosta & Huber, 2020). The Western Ghats are shown to be important drivers of orographic precipitation in this region, supplying runoff into the eastern Arabian Sea (Xie et al., 2006). A study of $^{40}Ar/^{39}Ar$ ages in the Western Ghats has shown that weathering and denudation has been active since at least the middle Eocene (~44 Ma; Bonnet et al., 2016; Jean et al., 2020). Modeling studies suggest that African and Arabian topography impact the strength and pattern of the Somali Jet but with only small effects on the spatial pattern, strength and seasonality of SAM precipitation (Chakraborty et al., 2009; Wei & Bordoni, 2016). These modeling studies therefore suggest that the tectonic/topographic configuration required for an active monsoon system (in terms of atmospheric circulation) in the Arabian Sea region has been present since at least the middle Eocene. However, it is unclear when the SAM atmospheric circulation and runoff intensified enough to have a strong impact on the Arabian Sea such that it became the dominant control on ocean circulation, salinity and oxygen content in the region.

5.4. The Late Phase of the Oligocene-Miocene Transition (23.0–22.7 Ma)

Coincident with the Oligocene-Miocene boundary (~23 Ma) there is a distinctive change in the sediment color at Site NGHP-01-01A, from a carbonate-rich, green/gray nannofossil ooze in the Oligocene to a brown, clay-rich ooze in the Miocene (~240 mbsf; Figure 4). Associated with this observed sedimentological change is: (a) a step increase in Ti/Ca counts suggesting a relative increase in the terrigenous fraction (Figures 7 and 9); (b) a decrease in $CaCO_3$ wt% (Figure 9a); (c) significant decreases in XRF-derived Mn/Fe and Mn/Ti ratios (Figure 7); and (d) a small decrease in planktic Mn/Ca (Figure 9f; Betzler et al., 2016; Bialik et al., 2020). Previous investigations of clay mineralogy at this site are at a much lower resolution but show that between ~228–240 mbsf (~23.0–19.0 Ma) smectite within the core makes up ~80% of the smectite versus kaolinite fraction, whilst ~250–280 mbsf (prior to 23 Ma) it only made up ~50% (Phillips et al., 2014). Illite also shows a step-increase from 0% to ~50% of the illite versus chlorite fraction at ~23 Ma (Phillips et al., 2014). Given the low resolution, these changes occurred sometime between ~25 and 23 Ma (Phillips et al., 2014). Within the Arabian Sea, provenance studies from the Holocene to Miocene have shown that smectite and illite are derived from the weathering of the Deccan province in western India and transported to the Arabian Sea via the Indus fan. Hence, these data may suggest a general increase in contribution from the weathering of NW India and/or the Himalayas to the eastern Arabian Sea (Alizai et al., 2012; Cai et al., 2018; Chen et al., 2019, 2020; Limmer et al., 2012; Yu et al., 2019) from the late Oligocene to early Miocene (Phillips et al., 2014). However, high-resolution provenance data for this site are required to support this hypothesis.

Coincident with the relative increase in terrigenous input (i.e., increased Ti/Ca) at the Arabian Sea site, there is a contemporaneous long-term decrease in sedimentation rate from 0.6 cm kyr^{-1} in the late Oligocene to 0.25 cm kyr^{-1} in the early Miocene (Figure 7b). The decrease in sedimentation rate would suggest that the observed sedimentological changes are driven by a relative reduction in $CaCO_3$ deposition (as opposed to, or in addition to, an actual increase in clay input), beginning at the Oligocene-Miocene boundary (~23 Ma) and continuing into the early Miocene. This assertion is supported by the steady rate of terrigenous flux throughout this interval suggesting terrigenous supply to this site remained unbroken into the early Miocene (Figure 7a), although we note that sedimentation at a single site cannot be considered representative of the region as a whole. There is also a transient decrease in $CaCO_3$ preservation shown by the significant fall in average %CF (Figure 6c), as well as the less well-preserved foraminifera observed under SEM during these low %CF intervals (Figure 3). Benthic foraminifera *C.* cf. *mundulus* shows enlarged pores (Figure 3d) and planktic foraminifera *D. venezuelana* displays encrusted/overgrown pores (Figure 3c), both indicative of minor dissolution/recrystallization. Enlarged pores of epibenthic foraminifera has also been shown to be a proxy for reduced bottom water oxygen (Rathburn et al., 2018), supporting the inference of reduced oxygenation during this interval. Importantly, although there seems to be some dissolution of foraminifera in the low %CF intervals this has not systematically biased either the isotope or trace element data (e.g., to lower Mg/Ca values; Figure S5). An apparent offset between the decline in $CaCO_3$ wt% data and XRF-derived Ca counts specifically in the interval 23.0–22.7 Ma (Figure 6a) is possibly due to the presence of Ca within smectite clays enhancing XRF-derived Ca. This $CaCO_3$–Ca offset therefore supports our interpretation of a decrease in carbonate fraction (biogenic calcite) and concurrent relative increase in (likely smectite dominated) clays at 23.0–22.7 Ma.

The most harmonious explanation for a simultaneous dissolution event (reduced $CaCO_3$ and preservation), decrease in oxygenation (Mn/Ca and sedimentary Mn), and a relative increase in terrigenous material (possibly driven by a change in chemical weathering) in the earliest Miocene (23.0–22.7 Ma; Figure 9) is a strengthening of SASM-like conditions in the Arabian Sea, such that the impacts are observed at Site NGHP-01-01A. The SASM under modern oceanographic conditions induces an intense OMZ in the north, central and eastern Arabian Sea due to strong southwest winds causing upwelling and productivity in the western Arabian Sea (Figure 2c). The Arabian Sea OMZ is present at intermediate depths (between ~150–1,250 m depth in the modern; Lachkar et al., 2018; Reichart, Nortier, et al., 2002). Although the Arabian Sea OMZ is partly driven by seasonal summer upwelling and high productivity, it is present throughout the year (McCreary et al., 2013), however observations suggest a seasonally decreased southward and westward extent during the SAWM (Shenoy et al., 2020). Intriguingly, the zone of high productivity is in the west, but the most intense part of the OMZ is in the north and east of the Arabian Sea; although a number of theories have been put forward to explain this offset between upwelling and deoxygenation zones, it remains

enigmatic (Shenoy et al., 2020). *D. venezuelana* was a thermocline dwelling species (Matsui et al., 2016; Stewart et al., 2012; Wade & Pälike, 2004), therefore likely inhabiting the upper part of our proposed OMZ through the early Miocene. The apparent dissolution of foraminifera at ~23.0–22.0 Ma could either be due to increased CO_2 (acidification) in the water column from high productivity/organic carbon flux and associated biotic respiration in surface waters (Lombard et al., 2010; Mungekar et al., 2020) and/or respiratory dissolution of carbonates on the seafloor due to increased organic carbon burial (Mawbey & Lear, 2013; Stewart et al., 2017).

The main terrigenous input to Site NGHP-01-01A today is via rivers flowing off the Western Ghats. Although many of the rivers originating in the Western Ghats flow to the east into the Bay of Bengal, several small rivers flow west into the Arabian Sea (Yang et al., 2020). As such, we expect terrigenous material derived from our proposed increase in the SASM at the Oligocene-Miocene boundary to have a provenance indicative of the Deccan Traps region (e.g., Cai et al., 2018; Chen et al., 2019, 2020; Clift et al., 2020; Phillips et al., 2014; Yu et al., 2019). Without quantitative provenance data such as neodymium isotopes (to constrain weathering source) we are unable to unequivocally state that the increase in weathering products (e.g., Ti) were sourced from the Deccan Traps. Future work will aim to constrain provenance changes and weathering fluxes from the hinterland through this time interval.

The deglaciation phase of the OMT (~23.0–22.7 Ma; Mawbey & Lear, 2013) is characterized by high-amplitude variability in short (~100-kyr) eccentricity cycles (Liebrand et al., 2017), in contrast to the low variability during the onset of the OMT glaciation period (Miller et al., 1991; Zachos et al., 2001). This is reflected in the amplitude of benthic oxygen isotope records at this time (Liebrand et al., 2016, 2017; Zachos et al., 2001). This change in orbital configuration could be the driving mechanism behind this intensification of the SAM (especially the SASM) over this deglaciation interval. An increase in orbital variability may trigger high frequency variability in atmospheric CO_2, perhaps not observed in currently available supra-orbital scale records of pCO_2 over the Oligocene and early Miocene (Figure 1e; Greenop et al., 2017, 2019; Grein et al., 2013; Liebrand et al., 2017; Londoño et al., 2018; Steinthorsdottir et al., 2019; Tesfamichael et al., 2017; Zhang et al., 2013). General circulation modeling suggests increased pCO_2 is linked to increased SAM precipitation amount and area (Kitoh et al., 2013; Turner & Annamalai, 2012) as well as stronger atmospheric winds blowing northwards in the Indian sector (Cherchi et al., 2011), thus suggesting increased CO_2 during the Oligocene-Miocene may have driven the observed changes at Site NGHP-01-01A.

Our data record no clear change in $\delta^{18}O_{sw}$ over the OMT, which would be an indicator of an intensification of monsoonal precipitation in the eastern Arabian Sea and/or increased monsoon-driven runoff from peninsular India. Despite this, there is a significant decrease in planktic foraminiferal $\delta^{18}O$ values (Figure 6e). This disparity in oxygen isotope trends suggests there was no change in the evaporation-precipitation balance at this site, despite the development of an intense OMZ suggesting monsoonal atmospheric circulation was active from at least the earliest Miocene. As *D. venezuelana* is a thermocline dwelling species during this interval it is possible that the effects of changes in surface ocean evaporation-precipitation balance was not transmitted to these depths. Our data therefore suggest an intensification of a proto-summer SAM based upon the influence of the monsoon systems on the thermocline and deep waters in this region, not on the sea surface.

5.5. Long-Term Shift in Sedimentology at Site NGHP-01-01A

Several modeling studies have suggested that the SAM has been active since at least the early Eocene (e.g., Acosta & Huber, 2020; Farnsworth et al., 2019; Huber & Goldner, 2012). Based on our data from the eastern Arabian Sea, the Oligocene-Miocene boundary was a key interval of strengthening of this proto-monsoon system. This suggests that perhaps there was a long-term shift in climatic/tectonic/orbital conditions, which triggered the intensification of a proto-SAM wind system over this interval (i.e., a well-developed OMZ in the eastern Arabian Sea), implying a strong Somali/Findlater jet (monsoonal atmospheric circulation). A number of possibilities arise for a long-term strengthening of a proto-SAM through this interval, evidenced from the decrease in biogenic calcite (decreased $CaCO_3$ wt% and XRF-derived Ca), occurrence of a well-developed OMZ (decrease in Mn) and possible increase in chemical weathering products (smectite) from 23 Ma onwards (Figure 9). These possibilities are discussed below.

It has been suggested that as India transitioned northwards to its current position, it moved through the ITCZ during the early Miocene (Armstrong & Allen, 2011; Beaumont et al., 2001; Clift et al., 2008). This movement not only initiated more intense monsoonal rainfall but may have also created a feedback, which initiated elevated Himalayan exhumation rates (due to increased denudation and subsequent lithospheric unloading). This is supported by the existence of a large unconformity in Himalayan sedimentary sequences spanning the Oligocene-early Miocene interval, possibly due to high rates of erosion of the Himalayas (Clift & Vanlaningham, 2010). Modeling of Eocene boundary conditions also showed that this northward movement of India through the ITCZ acted to redistribute moisture convergence in the region (Huber & Goldner, 2012). As India continued to move further north into its current position, a more seasonal, modern monsoon system would have been established (Allen & Armstrong, 2012; Armstrong & Allen, 2011).

Alternatively, the retreat of the Paratethys Sea (a restricted sub-basin of the Tethys Ocean), due to Himalayan-Tibetan Plateau uplift, is thought to have facilitated a shift from a temperate to continental climate in central Eurasia, causing a subsequent drying of this area (Fluteau et al., 1999; Ramstein et al., 1997). This would have provided a source of aeolian dust to be transported to the Arabian Sea and northern Indian Ocean, predominantly by north-easterly winter monsoon winds (Aston et al., 1973; Betzler et al., 2016). However, the flux of aeolian material to the eastern Arabian Sea is thought to be negligible compared to fluvially derived terrigenous materials (Clemens & Prell, 1990, 1991). Estimates vary for when central Eurasian desertification may have occurred, yet several Central Asian loess and paleobotanical records are dated to the late Oligocene to early Miocene interval (Guo et al., 2002; Licht et al., 2016; Lu & Guo, 2014; Qiang et al., 2011; X. Sun & Wang, 2005; Zheng et al., 2015).

Finally, changes in orbital configuration drive changes in insolation at the Earth's surface which in turn affects the hydrological cycle. During the Oligocene, periods of global warmth (indicated by benthic oxygen isotope compilations) coincided with times of high insolation in the Northern Hemisphere (i.e., perihelion in Northern Hemisphere summer), whereas global warmth during the Miocene occurred during times of both Northern and Southern Hemisphere high insolation (De Vleeschouwer et al., 2017). The early Miocene interval was also a time of high amplitude variability in short eccentricity (Liebrand et al., 2017). These changes in orbital forcing are proposed to have driven changes in Antarctic ice volume and atmospheric CO_2 on astronomical timescales (De Vleeschouwer et al., 2017, 2020), with the latter having a potential impact on the global and regional hydrological cycle (Carmichael et al., 2016; Lu & Guo, 2014; Yang et al., 2003) and subsequently the monsoon systems.

Given that tectonic movements are relatively slow, and the apparent increase in proto-monsoon intensity at the Oligocene-Miocene boundary in our records occurs over <500 kyr, it is likely that the sudden step-change we observe in the eastern Arabian Sea at ~23 Ma is primarily due to orbitally forced climatic factors superimposed on long-term regional tectonic forcing of oceanic gateways and uplift. The strengthening of a proto-SAM system by the earliest Neogene is supported by fossil megaflora in India (Srivastava et al., 2012), dust provenance studies from the Maldives (Betzler et al., 2016), enhanced weathering of the Western Ghats at the Oligocene-Miocene boundary (Bonnet et al., 2016; Jean et al., 2020), a major Oligocene-Miocene unconformity in the Himalayan foreland basin (Clift & Vanlaningham, 2010), increased erosion of the Himalayan foreland basin evidenced from thermochronology data (Clift et al., 2008; Webb et al., 2017), and increased SAM precipitation observed in a recent modeling study (Thomson et al., 2021). Data from the same Site NGHP-01-01A from the middle Miocene show a major strengthening in SAM precipitation and runoff from ~15 Ma (Yang et al., 2020). Our records now also show a strengthening of a proto-SAM system at the Oligocene-Miocene transition.

6. Conclusions

The sedimentary sequence from eastern Arabian Sea site NGHP-01-01A is the first marine record to cover the Oligocene to early Miocene interval in this region, helping to fill a critical gap in our knowledge of this time period. We employ a multi-proxy approach, including core scanning X-ray fluorescence data to investigate bulk sediment elemental composition, as well as foraminiferal geochemistry (stable isotopes and trace elements). According to foraminiferal stable isotope compositions ($\delta^{13}C$, $\delta^{18}O$), the isotopic records from this site are commensurate with other low latitude sites through this time interval, following broadly the global

trends, especially in benthic carbon isotopes. Throughout the Oligocene and early Miocene interval warm subtropical thermocline temperatures persisted (~25–32°C), with climate events such as the late Oligocene warming event and OMT not being particularly prominent, similar to other records from the low latitudes.

During the earliest part of the OMT (23.7–23.0 Ma) there was an increase in water column mixing and ventilation at this site, possibly driven by an increase in winter monsoon-type atmospheric circulation. This is evidenced by a reduction in $\Delta\delta^{13}C$, increase in bulk sediment Mn/Fe and Mn/Ti and foraminiferal Mn/Ca (signaling increased oxygenation), and good $CaCO_3$ preservation. We suggest this change was driven by a southward shift of the intertropical convergence zone over the peak of OMT glaciation due to the occurrence of an extended period of low eccentricity orbits (Liebrand et al., 2017; Zachos et al., 2001). Coincident with the Oligocene-Miocene boundary in the latter part of the OMT (~23.0 Ma) there was a long-term change in sedimentation at this site. A reduction in $CaCO_3$ and percentage coarse fraction, rise in Ti/Ca, high smectite (possible weathering products of the Deccan Traps), and relative reduction in bulk sediment Mn/Fe and Mn/Ti (reduced oxygenation) all suggest that this step-change was caused by a strengthening of a proto-summer SAM system and associated development of an intense oxygen minimum zone. It is evident from middle Miocene age data from this site that there was a major intensification of the South Asian summer monsoon coinciding with the middle Miocene climate transition (Yang et al., 2020). Overall, our new data suggests an earlier intensification of a proto-SAM at the Oligocene-Miocene boundary.

Conflict of interest

The authors declare no conflicts of interest relevant to this study.

Data Availability Statement

All data presented in this manuscript are available on Pangaea (https://doi.org/10.1594/PANGAEA.931901).

Acknowledgments
This research forms part of a PhD study funded by the Natural Environment Research Council (NERC) Centre for Doctoral Training in Oil & Gas (grant number NE/M00578X/1) awarded to C. Beasley, and was also supported by a NERC National Environmental Isotope Facility Steering Committee grant (IP-1865-1118) awarded to S. Kender. L. Giosan acknowledges funding from USSP and WHOI and thanks colleagues from the NGHP-01 expedition. C. Ullmann acknowledges funding via NERC grant NE/N018508/1. We thank Joe Stewart and Or Bialik for interesting and fruitful discussions of initial datasets. Thanks also go to two anonymous reviewers and Alex Farnsworth (AE), whose comments and suggestions greatly improved the manuscript.

References

Acharya, S. S., & Panigrahi, M. K. (2016). Eastward shift and maintenance of Arabian Sea oxygen minimum zone: Understanding the paradox. *Deep-Sea Research Part I: Oceanographic Research Papers*, *115*, 240–252. https://doi.org/10.1016/j.dsr.2016.07.004

Acosta, R. P., & Huber, M. (2020). Competing topographic mechanisms for the summer Indo-Asian Monsoon. *Geophysical Research Letters*, *47*, 1–11. https://doi.org/10.1029/2019GL085112

Alizai, A., Hillier, S., Clift, P. D., Giosan, L., Hurst, A., Van Laningham, S., & Macklin, M. (2012). Clay mineral variations in Holocene terrestrial sediments from the Indus Basin. *Quaternary Research*, *77*, 368–381. https://doi.org/10.1016/j.yqres.2012.01.008

Allen, M. B., & Armstrong, H. A. (2012). Reconciling the intertropical convergence zone, Himalayan/Tibetan tectonics, and the onset of the Asian monsoon system. *Journal of Asian Earth Sciences*, *44*, 36–47. https://doi.org/10.1016/j.jseaes.2011.04.018

Anand, P., Elderfield, H., & Conte, M. H. (2003). Calibration of Mg/Ca thermometry in planktonic foraminifera from a sediment trap time series. *Paleoceanography*, *18*(2), 1050. https://doi.org/10.1029/2002pa000846

Anderson, D. M., & Prell, W. L. (1993). A 300 kyr record of upwelling off Oman during the Late Quaternary: Evidence of the Asian southwest monsoon. *Paleoceanography*, *8*(2), 193–208. https://doi.org/10.1029/93pa00256

Armstrong, H. A., & Allen, M. B. (2011). Shifts in the intertropical convergence zone, Himalayan exhumation, and late Cenozoic climate. *Geology*, *39*(1), 11–14. https://doi.org/10.1130/G31005.1

Aston, S. R., Chester, R., Johnson, L. R., & Padgham, R. C. (1973). Eolian dust from the lower atmosphere of the eastern Atlantic and Indian Oceans, China Sea and Sea of Japan. *Marine Geology*, *14*, 15–28. https://doi.org/10.1016/0025-3227(73)90040-6

Barras, C., Mouret, A., Nardelli, M. P., Metzger, E., Petersen, J., La, C., et al. (2018). Experimental calibration of manganese incorporation in foraminiferal calcite. *Geochimica et Cosmochimica Acta*, *237*, 49–64. https://doi.org/10.1016/j.gca.2018.06.009

Beaumont, C., Jamieson, R. A., Nguyen, M. H., & Lee, B. (2001). Himalayan tectonics explained by extrusion of a low-viscosity crustal channel coupled to focused surface denudation. *Nature*, *414*, 738–742. https://doi.org/10.1038/414738a

Beddow, H. M., Liebrand, D., Sluijs, A., Wade, B. S., & Lourens, L. J. (2016). Global change across the Oligocene–Miocene transition: High-resolution stable isotope records from IODP Site U1334 (equatorial Pacific Ocean). *Paleoceanography*, *31*, 81–97. https://doi.org/10.1002/2015PA002820

Beddow, H. M., Liebrand, D., Wilson, D. S., Hilgen, F. J., Sluijs, A., Wade, B. S., & Lourens, L. J. (2018). Astronomical tunings of the Oligocene–Miocene transition from Pacific Ocean Site U1334 and implications for the carbon cycle. *Climate of the Past*, *14*(3), 255–270. https://doi.org/10.5194/cp-14-255-2018

Bemis, B. E., Spero, H. J., Bijma, J., & Lea, D. W. (1998). Reevaluation of the oxygen isotopic composition of planktonic foraminifera: Experimental results and revised paleotemperature equations. *Paleoceanography*, *13*(2), 150–160. https://doi.org/10.1029/98PA00070

Bergen, J., de Kaenel, E., Blair, S., Boesiger, T., & Browning, E. (2017). Oligocene–Pliocene taxonomy and stratigraphy of the genus *Sphenolithus* in the circum North Atlantic Basin: Gulf of Mexico and ODP Leg 154. *Journal of Nannoplankton Research*, *37*(2–3), 77–112.

Bertrand, S., Hughen, K. A., Sepúlveda, J., & Pantoja, S. (2012). Geochemistry of surface sediments from the fjords of Northern Chilean Patagonia (44–47°S): Spatial variability and implications for paleoclimate reconstructions. *Geochimica et Cosmochimica Acta*, *76*, 125–146. https://doi.org/10.1016/j.gca.2011.10.028

Betzler, C., Eberli, G. P., Kroon, D., Wright, J. D., Swart, P. K., Nath, B. N., et al. (2016). The abrupt onset of the modern South Asian Monsoon winds. *Scientific Reports*, *6*, 1–10. https://doi.org/10.1038/srep29838

Bialik, O. M., Auer, G., Ogawa, N. O., Kroon, D., Waldmann, N. D., & Ohkouchi, N. (2020). Monsoons, upwelling, and the deoxygenation of the Northwestern Indian Ocean in response to middle to late miocene global climatic shifts. *Paleoceanography and Paleoclimatology*, *35*(2), 1–17. https://doi.org/10.1029/2019pa003762

Bischoff, T., & Schneider, T. (2014). Energetic constraints on the position of the intertropical convergence zone. *Journal of Climate*, *27*, 4937–4951. https://doi.org/10.1175/JCLI-D-13-00650.1

Böning, P., & Bard, E. (2009). Millennial/centennial-scale thermocline ventilation changes in the Indian Ocean as reflected by aragonite preservation and geochemical variations in Arabian Sea sediments. *Geochimica et Cosmochimica Acta*, *73*, 6771–6788. https://doi.org/10.1016/j.gca.2009.08.028

Bonnet, N. J., Beauvais, A., Arnaud, N., Chardon, D., & Jayananda, M. (2016). Cenozoic lateritic weathering and erosion history of Peninsular India from 40Ar/39Ar dating of supergene K–Mn oxides. *Chemical Geology*, *446*, 33–53. https://doi.org/10.1016/j.chemgeo.2016.04.018

Boos, W. R., & Kuang, Z. (2010). Dominant control of the South Asian monsoon by orographic insulation versus plateau heating. *Nature Letters*, *463*, 218–222. https://doi.org/10.1038/nature08707

Boos, W. R., & Kuang, Z. (2013). Sensitivity of the South Asian monsoon to elevated and non-elevated heating. *Scientific Reports*, *3*(1192), 1–4. https://doi.org/10.1038/srep01192

Bordoni, S., & Schneider, T. (2008). Monsoon as eddy-mediated regime transitions of the tropical overturning circulation. *Nature Geoscience*, *1*, 515–519. https://doi.org/10.1038/ngeo248

Bown, P. R., & Young, J. R. (1998). Techniques. In P. R. Bown (Ed.), *Calcareous nannofossil biostratigraphy* (pp. 16–28). Kluwer Academic. https://doi.org/10.1007/978-94-011-4902-0_2

Boyle, E. A., & Keigwin, L. D. (1985). Comparison of Atlantic and Pacific paleochemical records for the last 215,000 years: Changes in deep ocean circulation and chemical inventories. *Earth and Planetary Science Letters*, *76*, 135–150. https://doi.org/10.1016/0012-821X(85)90154-2

Broccoli, A. J., Dahl, K. A., & Stouffer, R. J. (2006). Response of the ITCZ to Northern Hemisphere cooling. *Geophysical Research Letters*, *33*, 1–4. https://doi.org/10.1029/2005GL024546

Cai, M., Xu, Z., Clift, P. D., Khim, B. K., Lim, D., Yu, Z., et al. (2018). Long-term history of sediment inputs to the eastern Arabian Sea and its implications for the evolution of the Indian summer monsoon since 3.7 Ma. *Geological Magazine*, *157*, 1–12. https://doi.org/10.1017/S0016756818000857

Campbell, S. M., Moucha, R., Derry, L. A., & Raymo, M. E. (2018). Effects of dynamic topography on the cenozoic carbonate compensation depth. *Geochemistry, Geophysics, Geosystems*, *19*, 1025–1034. https://doi.org/10.1002/2017GC007386

Carmichael, M. J., Lunt, D. J., Huber, M., Heinemann, M., Kiehl, J., LeGrande, A., et al. (2016). A model-model and data-model comparison for the early Eocene hydrological cycle. *Climate of the Past*, *12*(2), 455–481. https://doi.org/10.5194/cp-12-455-2016

Chakraborty, A., Nanjundiah, R. S., & Srinivasan, J. (2009). Impact of African orography and the Indian summer monsoon on the low-level Somali jet. *International Journal of Climatology*, *29*, 983–992. https://doi.org/10.1002/joc10.1002/joc.1720

Chen, H., Xu, Z., Clift, P. D., Lim, D., Khim, B. K., & Yu, Z. (2019). Orbital-scale evolution of the Indian summer monsoon since 1.2 Ma: Evidence from clay mineral records at IODP Expedition 355 Site U1456 in the eastern Arabian Sea. *Journal of Asian Earth Sciences*, *174*, 11–22. https://doi.org/10.1016/j.jseaes.2018.10.012

Chen, H., Xu, Z., Lim, D., Clift, P. D., Chang, F., Li, T., et al. (2020). Geochemical records of the provenance and silicate weathering/erosion from the Eastern Arabian Sea and their responses to the indian summer monsoon since the Mid-Pleistocene. *Paleoceanography and Paleoclimatology*, *35*, 1–18. https://doi.org/10.1029/2019PA003732

Cherchi, A., Alessandri, A., Masina, S., & Navarra, A. (2011). Effects of increased CO_2 levels on monsoons. *Climate Dynamics*, *37*, 83–101. https://doi.org/10.1007/s00382-010-0801-7

Clemens, S. C., & Prell, W. L. (1990). Late Pleistocene variability of Arabian Sea summer monsoon winds and continental aridity: Eolian records from the lithogenic component of deep-sea sediments. *Paleoceanography*, *5*(2), 109–145. https://doi.org/10.1029/pa005i002p00109

Clemens, S. C., & Prell, W. L. (1991). One million year record of summer monsoon winds and continental aridity from the Owen Ridge (Site 722), Northwest Arabian Sea. *Proceedings of the Ocean Drilling Program, Scientific Results*, *117*, 365–388. https://doi.org/10.2973/odp.proc.sr.117.138.1991

Clift, P. D., Hodges, K. V., Heslop, D., Hannigan, R., Van Long, H., & Calves, G. (2008). Correlation of Himalayan exhumation rates and Asian monsoon intensity. *Nature Geoscience*, *1*, 875–880. https://doi.org/10.1038/ngeo351

Clift, P. D., Kroon, D., Gaedicke, C., & Craig, J. (2002). *Tectonic and Climatic Evolution of The Arabian Sea Region: An Introduction* (Vol. 195, pp. 1–5). Geological Society Special Publications. https://doi.org/10.1144/GSL.SP.2002.195.01.01

Clift, P. D., Kulhanek, D. K., Zhou, P., Bowen, M. G., Vincent, S. M., Lyle, M., & Hahn, A. (2020). Chemical weathering and erosion responses to changing monsoon climate in the Late Miocene of Southwest Asia. *Geological Magazine*, *157*, 939–955. https://doi.org/10.1017/S0016756819000608

Clift, P. D., & Van laningham, S. (2010). A climatic trigger for a major Oligo–Miocene unconformity in the Himalayan foreland basin. *Tectonics*, *29*, 1–n. https://doi.org/10.1029/2010TC002711

Clift, P. D., & Webb, A. G. (2019). A history of the Asian monsoon and its interactions with solid Earth tectonics in Cenozoic South Asia. In P. J. Treloar, & M. P. Searle (Eds.), Himalayan Tectonics: A Modern Synthesis (Vol. 483, pp. 631–652). Geological Society, London, Special Publications. https://doi.org/10.1144/sp483.1

Collett, T. S., Riedel, M., Cochran, J. R., Boswell, R., Presley, J., Kumar, P., et al. (2008). National gas hydrate Program expedition 01 initial reports. *Directorate General of Hydrocarbons*. New Delhi.

Coxall, H. K., Wilson, P. A., Pälike, H., Lear, C. H., & Backman, J. (2005). Rapid stepwise onset of Antarctic glaciation and deeper calcite compensation in the Pacific Ocean. *Nature*, *433*, 53–57. https://doi.org/10.1038/nature03135

Davis, C. V., & Benitez-Nelson, C. R. (2020). Evidence for rapid trace element alteration of planktic foraminiferal shells from the Panama Basin: Manganese adsorption during vertical transport. *Marine Micropaleontology*, *157*, 101872. https://doi.org/10.1016/j.marmicro.2020.101872

de la Vara, A., Meijer, P. T., & Wortel, M. J. R. (2013). Model study of the circulation of the Miocene Mediterranean Sea and Paratethys: Closure of the Indian Gateway. *Climate of the Past Discussions*, *9*, 4385–4424. https://doi.org/10.5194/cpd-9-4385-2013

De Vleeschouwer, D., Drury, A. J., Liebrand, D., Pälike, H., Vahlenkamp, M., & Rochholz, F. (2020). High-latitude biomes and rock weathering mediate climate-carbon cycle feedbacks on eccentricity timescales. *Nature Communications*, *11*(5013), 1–10. https://doi.org/10.1038/s41467-020-18733-w

De Vleeschouwer, D., Vahlenkamp, M., Crucifix, M., & Pälike, H. (2017). Alternating Southern and Northern Hemisphere climate response to astronomical forcing during the past 35 m.y. *Geology*, *45*(4), 375–378. https://doi.org/10.1130/G38663.1

Dickens, G. R., & Owen, R. M. (1994). Late Miocene–early Pliocene manganese redirection in the central Indian Ocean: Expansion of the intermediate water oxygen minimum zone. *Paleoceanography*, *9*(1), 169–181. https://doi.org/10.1029/93PA02699

Dimri, A. P., Yasunari, T., Kotlia, B. S., Mohanty, U. C., & Sikka, D. R. (2016). Indian winter monsoon: Present and past. *Earth-Science Reviews*, *163*, 297–322. https://doi.org/10.1016/j.earscirev.2016.10.008

Ding, L., Spicer, R. A., Yang, J., Xu, Q., Cai, F., Li, S., et al. (2017). Quantifying the rise of the Himalaya orogen and implications for the South Asian monsoon. *Geology*, *45*(3), 215–218. https://doi.org/10.1130/G38583.1

Drury, A. J., Liebrand, D., Westerhold, T., Beddow, H. M., Hodell, D. A., Rohlfs, N., et al. (2020). Climate, cryosphere and carbon cycle controls on Southeast Atlantic orbital-scale carbonate deposition since the Oligocene (30–0 Ma). *Climate of the Past*, accepted, 1–35. https://doi.org/10.5194/cp-2020-108

Edgar, K. M., Pälike, H., & Wilson, P. A. (2013). Testing the impact of diagenesis on the $\delta^{18}O$ and $\delta^{13}C$ of benthic foraminiferal calcite from a sediment burial depth transect in the equatorial Pacific. *Paleoceanography*, *28*, 468–480. https://doi.org/10.1002/palo.20045

Egger, L. M., Bahr, A., Friedrich, O., Wilson, P. A., Norris, R. D., van Peer, T. E., et al. (2018). Sea-level and surface-water change in the western North Atlantic across the Oligocene–Miocene Transition: A palynological perspective from IODP Site U1406 (Newfoundland margin). *Marine Micropaleontology*, *139*, 57–71. https://doi.org/10.1016/j.marmicro.2017.11.003

Elderfield, H., & Ganssen, G. (2000). Past temperature and $\delta^{18}O$ of surface ocean waters inferred from foraminiferal Mg/Ca ratios. *Nature*, *405*, 442–445. https://doi.org/10.1038/35013033

Evans, D., Brierley, C., Raymo, M. E., Erez, J., & Müller, W. (2016). Planktic foraminifera shell chemistry response to seawater chemistry: Pliocene–Pleistocene seawater Mg/Ca, temperature and sea level change. *Earth and Planetary Science Letters*, *438*, 139–148. https://doi.org/10.1016/j.epsl.2016.01.013

Evans, D., Sagoo, N., Renema, W., Cotton, L. J., Müller, W., Todd, J. A., et al. (2018). Eocene greenhouse climate revealed by coupled clumped isotope-Mg/Ca thermometry. *Proceedings of the National Academy of Sciences of the United States of America*, *115*(6), 1174–1179. https://doi.org/10.1073/pnas.1714744115

Evans, D., Wade, B. S., Henehan, M., Erez, J., & Müller, W. (2016). Revisiting carbonate chemistry controls on planktic foraminifera Mg/Ca: Implications for sea surface temperature and hydrology shifts over the Paleocene–Eocene Thermal Maximum and Eocene–Oligocene transition. *Climate of the Past*, *12*, 819–835. https://doi.org/10.5194/cp-12-819-2016

Farnsworth, A., Lunt, D. J., Robinson, S. A., Valdes, P. J., Roberts, W. H. G., Clift, P. D., et al. (2019). Past East Asian monsoon evolution controlled by paleogeography, not CO_2. *Science Advances*, *5*(10), 1–14. https://doi.org/10.1126/sciadv.aax1697

Findlater, J. (1969). A major low-level air current near the Indian Ocean during the northern summer. *Quarterly Journal of the Royal Meteorological Society*, *95*, 362–380. https://doi.org/10.1002/qj.49709540409

Flores, J. A., Johnson, J. E., Mejía-Molina, A. E., Álvarez, M. C., Sierro, F. J., Singh, S. D., et al. (2014). Sedimentation rates from calcareous nannofossil and planktonic foraminifera biostratigraphy in the Andaman Sea, northern Bay of Bengal, and eastern Arabian Sea. *Marine and Petroleum Geology*, *58*, 425–437. https://doi.org/10.1016/j.marpetgeo.2014.08.011

Fluteau, F., Ramstein, G., & Besse, J. (1999). Simulating the evolution of the Asian and African monsoons during the past 30 Myr using an atmospheric general circulation model. *Journal of Geophysical Research*, *104*(10), 11995–12018. https://doi.org/10.1029/1999jd900048

Fraass, A. J., Leckie, M. R., Lowery, C. M., & Deconto, R. (2019). Precision in biostratigraphy: Evidence for a temporary flow reversal in the Central American Seaway during or after the Oligocene–Miocene transition. *Journal of Foraminiferal Research*, *49*(4), 357–366. https://doi.org/10.2113/gsjfr.49.4.357

Gadgil, S. (2018). The monsoon system: Land-sea breeze or the ITCZ? *Journal of Earth System Science*, *127*(1). https://doi.org/10.1007/s12040-017-0916-x

Gradstein, F. M., Ogg, J. G., & Hilgen, F. J. (2012). On the geologic time scale. *Newsletters on Stratigraphy*, *45*(2), 171–188. https://doi.org/10.1127/0078-0421/2012/0020

Gray, W. R., & Evans, D. (2019). Nonthermal influences on Mg/Ca in planktonic Foraminifera: A review of culture studies and application to the last glacial maximum. *Paleoceanography and Paleoclimatology*, *34*, 306–315. https://doi.org/10.1029/2018PA003517

Greenop, R., Hain, M. P., Sosdian, S. M., Oliver, K. I. C., Goodwin, P., Chalk, T. B., et al. (2017). A record of Neogene seawater $\delta^{11}B$ reconstructed from paired $\delta^{11}B$ analyses on benthic and planktic foraminifera. *Climate of the Past*, *13*, 149–170. https://doi.org/10.5194/cp-13-149-2017

Greenop, R., Sosdian, S. M., Henehan, M. J., Wilson, P. A., Lear, C. H., & Foster, G. L. (2019). Orbital forcing, ice volume, and CO_2 across the oligocene–miocene transition. *Paleoceanography and Paleoclimatology*, *34*, 316–328. https://doi.org/10.1029/2018PA003420

Grein, M., Oehm, C., Konrad, W., Utescher, T., Kunzmann, L., & Roth-Nebelsick, A. (2013). Atmospheric CO_2 from the late Oligocene to early Miocene based on photosynthesis data and fossil leaf characteristics. *Palaeogeography, Palaeoclimatology, Palaeoecology*, *374*, 41–51. https://doi.org/10.1016/j.palaeo.2012.12.025

Guitián, J., Phelps, S., Polissar, P. J., Ausín, B., Eglinton, T. I., & Stoll, H. M. (2019). Midlatitude temperature variations in the Oligocene to early Miocene. *Paleoceanography and Paleoclimatology*, *34*, 1328–1343. https://doi.org/10.1029/2019PA003638

Guo, Z. T., Ruddiman, W. F., Hao, Q. Z., Wu, H. B., Qiao, Y. S., Zhu, R. X., et al. (2002). Onset of Asian desertification by 22 Myr ago inferred from loess deposits in China. *Nature*, *416*, 159–163. https://doi.org/10.1038/416159a

Guo, Z. T., Sun, B., Zhang, Z. S., Peng, S. Z., Xiao, G. Q., Ge, J. Y., et al. (2008). A major reorganization of Asian climate by the early Miocene. *Climate of the Past*, *4*, 153–174. https://doi.org/10.5194/cp-4-153-2008

Gupta, A. K., Prakasam, M., Dutt, S., Clift, P. D., & Yadav, R. R. (2020). Evolution and development of the Indian Monsoon. In N. Gupta, & S. K. Tandon (Eds.), *Geodynamics of the Indian plate* (pp. 499–535). https://doi.org/10.1007/978-3-030-15989-4_14

Gupta, A. K., Yuvaraja, A., Prakasam, M., Clemens, S. C., & Velu, A. (2015). Evolution of the South Asian monsoon wind system since the late Middle Miocene. *Palaeogeography, Palaeoclimatology, Palaeoecology*, *438*, 160–167. https://doi.org/10.1016/j.palaeo.2015.08.006

Hamon, N., Sepulchre, P., Lefebvre, V., & Ramstein, G. (2013). The role of eastern Tethys seaway closure in the Middle Miocene Climatic Transition (ca. 14 Ma). *Climate of the Past*, *9*, 2687–2702. https://doi.org/10.5194/cp-9-2687-2013

Horita, J., Zimmermann, H., & Holland, H. D. (2002). Chemical evolution of seawater during the Phanerozoic: Implications from the record of marine evaporites. *Geochimica et Cosmochimica Acta*, *66*(21), 3733–3756. https://doi.org/10.1016/S0016-7037(01)00884-5

Huber, M., & Goldner, A. (2012). Eocene monsoons. *Journal of Asian Earth Sciences*, *44*, 3–23. https://doi.org/10.1016/j.jseaes.2011.09.014

Hyeong, K., Lee, J., Seo, I., Lee, M. J., Yoo, C. M., & Khim, B. K. (2014). Southward shift of the Intertropical Convergence Zone due to Northern Hemisphere cooling at the Oligocene–Miocene boundary. *Geology*, *42*(8), 667–670. https://doi.org/10.1130/G35664.1

Jean, A., Beauvais, A., Chardon, D., Arnaud, N., Jayananda, M., & Mathe, P. E. (2020). Weathering history and landscape evolution of Western Ghats (India) from $^{40}Ar/^{39}Ar$ dating of supergene K–Mn oxides. *Journal of the Geological Society*, *177*, 523–536. https://doi.org/10.1144/jgs2019-048

Jiang, D., Ding, Z., Drange, H., & Gao, Y. (2008). Sensitivity of East Asian climate to the progressive uplift and expansion of the Tibetan Plateau under the mid-Pliocene boundary conditions. *Advances in Atmospheric Sciences*, *25*(5), 709–722. https://doi.org/10.1007/s00376-008-0709-x

Johnson, J. E., Phillips, S. C., Torres, M. E., Piñero, E., Rose, K. K., & Giosan, L. (2014). Influence of total organic carbon deposition on the inventory of gas hydrate in the Indian continental margins. *Marine and Petroleum Geology*, *58*, 406–424. https://doi.org/10.1016/j.marpetgeo.2014.08.021

Keigwin, L. D., & Corliss, B. H. (1986). Stable isotopes in late middle Eocene to Oligocene foraminifera. The *Geological Society of America Bulletin*, *97*, 335–345. https://doi.org/10.1130/0016-7606(1986)97<335:siilme>2.0.co;2

Kim, J. E., Khim, B. K., Ikehara, M., & Lee, J. (2018). Orbital-scale denitrification changes in the Eastern Arabian Sea during the last 800 kyrs. *Scientific Reports*, *8*, 1–8. https://doi.org/10.1038/s41598-018-25415-7

Kitoh, A., Endo, H., Kumar, K. K., Cavalcanti, I. F. A., Goswami, P., & Zhou, T. (2013). Monsoons in a changing world: A regional perspective in a global context. *Journal of Geophysical Research: Atmospheres*, *118*, 3053–3065. https://doi.org/10.1002/jgrd.50258

Kutzbach, J. E., Prell, W. L., & Ruddiman, W. F. (1993). Sensitivity of Eurasian climate to surface uplift of the Tibetan Plateau. *The Journal of Geology*, *101*(2), 177–190. https://doi.org/10.1086/648215

Lachkar, Z., Lévy, M., & Smith, S. (2018). Intensification and deepening of the Arabian Sea oxygen minimum zone in response to increase in Indian monsoon wind intensity. *Biogeosciences*, *15*, 159–186. https://doi.org/10.5194/bg-15-159-2018

Laskar, J., Robutel, P., Joutel, F., Gastineau, M., Correia, A. C. M., & Levrard, B. (2004). A long-term numerical solution for the insolation quantities of the Earth. *Astronomy and Astrophysics*, *428*, 261–285. https://doi.org/10.1051/0004-6361:20041335

Lear, C. H., Bailey, T. R., Pearson, P. N., Coxall, H. K., & Rosenthal, Y. (2008). Cooling and ice growth across the Eocene–Oligocene transition. *Geology*, *36*(3), 251–254. https://doi.org/10.1130/G24584A.1

Lear, C. H., Elderfield, H., & Wilson, P. A. (2000). Cenozoic deep-sea temperatures and global ice volumes from Mg/Ca in benthic foraminiferal calcite. *Science*, *287*, 269–272. https://doi.org/10.1126/science.287.5451.269

Lear, C. H., Rosenthal, Y., Coxall, H. K., & Wilson, P. A. (2004). Late Eocene to early Miocene ice sheet dynamics and the global carbon cycle. *Paleoceanography*, *19*, 1–n. https://doi.org/10.1029/2004PA001039

Lee, H., Jo, K.-N., & Hyun, S. (2020). Opposite response modes of NADW dynamics to obliquity forcing during the late Paleogene. *Scientific Reports*, *10*, 1–8. https://doi.org/10.1038/s41598-020-70020-2

Lee, J., Kim, S., & Khim, B. K. (2020). A paleoproductivity shift in the northwestern Bay of Bengal (IODP Site U1445) across the Mid-Pleistocene transition in response to weakening of the Indian summer monsoon. *Palaeogeography, Palaeoclimatology, Palaeoecology*, *560*, 110018. https://doi.org/10.1016/j.palaeo.2020.110018

Licht, A., Dupont-Nivet, G., Pullen, A., Kapp, P., Abels, H. A., Lai, Z., et al. (2016). Resilience of the Asian atmospheric circulation shown by Paleogene dust provenance. *Nature Communications*, *7*(12390), 1–6. https://doi.org/10.1038/ncomms12390

Licht, A., Van Cappelle, M., Abels, H. A., Ladant, J. B., Trabucho-Alexandre, J., France-Lanord, C., et al. (2014). Asian monsoons in a late Eocene greenhouse world. *Nature*, *513*, 501–506. https://doi.org/10.1038/nature13704

Liebrand, D., Beddow, H. M., Lourens, L. J., Pälike, H., Raffi, I., Bohaty, S. M., et al. (2016). Cyclostratigraphy and eccentricity tuning of the early Oligocene through early Miocene (30.1–17.1 Ma): *Cibicides mundulus* stable oxygen and carbon isotope records from Walvis Ridge Site 1264. *Earth and Planetary Science Letters*, *450*, 392–405. https://doi.org/10.1016/j.epsl.2016.06.007

Liebrand, D., de Bakker, A. T. M., Beddow, H. M., Wilson, P. A., Bohaty, S. M., Ruessink, G., et al. (2017). Evolution of the early Antarctic ice ages. *Proceedings of the National Academy of Sciences of the United States of America*, *114*(15), 3867–3872. https://doi.org/10.1073/pnas.1615440114

Liebrand, D., Lourens, L. J., Hodell, D. A., De Boer, B., Van De Wal, R. S. W., & Pälike, H. (2011). Antarctic ice sheet and oceanographic response to eccentricity forcing during the early Miocene. *Climate of the Past*, *7*, 869–880. https://doi.org/10.5194/cp-7-869-2011

Limmer, D. R., Köhler, C. M., Hillier, S., Moreton, S. G., Tabrez, A. R., & Clift, P. D. (2012). Chemical weathering and provenance evolution of Holocene–Recent sediments from the Western Indus Shelf, Northern Arabian Sea inferred from physical and mineralogical properties. *Marine Geology*, *326–328*, 101–115. https://doi.org/10.1016/j.margeo.2012.07.009

Littler, K., Röhl, U., Westerhold, T., & Zachos, J. C. (2014). A high-resolution benthic stable-isotope record for the South Atlantic: Implications for orbital-scale changes in Late Paleocene–Early Eocene climate and carbon cycling. *Earth and Planetary Science Letters*, *401*, 18–30. https://doi.org/10.1016/j.epsl.2014.05.054

Liu, Z., He, Y., Jiang, Y., Wang, H., Liu, W., Bohaty, S. M., & Wilson, P. A. (2018). Transient temperature asymmetry between hemispheres in the Palaeogene Atlantic Ocean. *Nature Geoscience*, *11*, 656–660. https://doi.org/10.1038/s41561-018-0182-9

Lombard, F., da Rocha, R. E., Bijma, J., & Gattuso, J. -P. (2010). Effect of carbonate ion concentration and irradiance on calcification in planktonic foraminifera. *Biogeosciences*, *7*, 247–255. https://doi.org/10.5194/bg-7-247-2010

Londoño, L., Royer, D. L., Jaramillo, C., Escobar, J., Foster, D. A., Cárdenas-Rozo, A. L., & Wood, A. (2018). Early Miocene CO_2 estimates from a Neotropical fossil leaf assemblage exceed 400 ppm. *American Journal of Botany*, *105*(11), 1929–1937. https://doi.org/10.1002/ajb2.1187

Lu, H. Y., & Guo, Z. T. (2014). Evolution of the monsoon and dry climate in East Asia during late Cenozoic: A review. *Science China Earth Sciences*, *57*(1), 70–79. https://doi.org/10.1007/s11430-013-4790-3

Matsui, H., Nishi, H., Takashima, R., Kuroyanagi, A., Ikehara, M., Takayanagi, H., & Iryu, Y. (2016). Changes in the depth habitat of the Oligocene planktic foraminifera (*Dentoglobigerina venezuelana*) induced by thermocline deepening in the eastern equatorial Pacific. *Paleoceanography*, *31*, 715–731. https://doi.org/10.1002/2016PA002950

Mawbey, E. M., & Lear, C. H. (2013). Carbon cycle feedbacks during the Oligocene–Miocene transient glaciation. *Geology*, *41*(9), 963–966. https://doi.org/10.1130/G34422.1

McCreary, J. P., Yu, Z., Hood, R. R., Vinaychandran, P. N., Furue, R., Ishida, A., & Richards, K. J. (2013). Dynamics of the Indian-Ocean oxygen minimum zones. *Progress in Oceanography*, *112–113*, 15–37. https://doi.org/10.1016/j.pocean.2013.03.002

Miller, K. G., Browning, J. V., Schmelz, W. J., Kopp, R. E., Mountain, G. S., & Wright, J. D. (2020). Cenozoic sea-level and cryospheric evolution from deep-sea geochemical and continental margin records. *Science Advances*, *6*, 1–15. https://doi.org/10.1126/sciadv.aaz1346

Miller, K. G., Wright, J. D., & Fairbanks, R. G. (1991). Unlocking the Ice House: Oligocene–Miocene oxygen isotopes, eustasy, and margin erosion. *Journal of Geophysical Research*, *96*(B4), 6829–6848. https://doi.org/10.1029/90JB02015

Mungekar, T. V., Naik, S. S., Nath, B. N., & Pandey, D. K. (2020). Shell weights of foraminifera trace atmospheric CO_2 from the Miocene to Pleistocene in the central Equatorial Indian Ocean. *Journal of Earth System Science*, *129*, 1–9. https://doi.org/10.1007/s12040-020-1348-6

Murray, R. W., Miller, D. J., & Kryc, K. A. (2000). Analysis of major and trace elements in rocks, sediments, and interstitial waters by inductively couple plasma-atomic emission spectrometry. *Technical Note #29, Ocean Drilling Program*, 27 pp.

O'Brien, C. L., Huber, M., Thomas, E., Pagani, M., Super, J. R., Elder, L. E., & Hull, P. M. (2020). The enigma of Oligocene climate and global surface temperature evolution. *Proceedings of the National Academy of Sciences of the United States of America*, *117*(41), 25302–25309. https://doi.org/10.1073/pnas.2003914117

Pälike, H., Norris, R. D., Herrle, J. O., Wilson, P. A., Coxall, H. K., Lear, C. H., et al. (2006). The heartbeat of the Oligocene climate system. *Science*, *314*, 1894–1898. https://doi.org/10.1126/science.1133822

Pandey, D. K., Clift, P. D., Kulhanek, D. K., Andò, S., Bendle, J. A. P., Bratenkov, S., et al. (2016). Expedition 355 summary. *Proceedings of the International Ocean Discovery Program*, *355*, 1–32. https://doi.org/10.14379/iodp.proc.355.101.2016

Parvathi, V., Suresh, I., Lengaigne, M., Izumo, T., & Vialard, J. (2017). Robust projected weakening of winter monsoon winds over the Arabian Sea under climate change. *Geophysical Research Letters*, *44*, 9833–9843. https://doi.org/10.1002/2017GL075098

Paul, H. A., Zachos, J. C., Flower, B. P., & Tripati, A. K. (2000). Orbitally induced climate and geochemical variability across the Oligocene/Miocene boundary. *Paleoceanography*, *15*(5), 471–485. https://doi.org/10.1029/1999pa000443

Pena, L. D., Calvo, E., Cacho, I., Eggins, S., & Pelejero, C. (2005). Identification and removal of Mn-Mg-rich contaminant phases on foraminiferal tests: Implications for Mg/Ca past temperature reconstructions. *Geochemistry, Geophysics, Geosystems*, *6*(9), 1–25. https://doi.org/10.1029/2005GC000930

Peterson, L. C., & Backman, J. (1990). Late Cenozoic carbonate accumulation and the history of the carbonate compensation depth in the western equatorial Indian Ocean. *Proceedings of the Ocean Drilling Program, Scientific Results*, *115*, 467–507. https://doi.org/10.2973/odp.proc.sr.115.163.1990

Phillips, S. C., Johnson, J. E., Underwood, M. B., Guo, J., Giosan, L., & Rose, K. (2014). Long-timescale variation in bulk and clay mineral composition of Indian continental margin sediments in the Bay of Bengal, Arabian Sea, and Andaman Sea. *Marine and Petroleum Geology*, *58*, 117–138. https://doi.org/10.1016/j.marpetgeo.2014.06.018

Prasanna Kumar, S., Narvekar, J., Kumar, A., Shaji, C., Anand, P., Sabu, P., et al. (2004). Intrusion of the Bay of Bengal water into the Arabian Sea during winter monsoon and associated chemical and biological response. *Geophysical Research Letters*, *31*, 1–4. https://doi.org/10.1029/2004GL020247

Privé, N. C., & Plumb, R. A. (2007). Monsoon Dynamics with Interactive Forcing. Part 2: Impact of eddies and asymmetric geometries. *Journal of the Atmospheric Sciences*, *64*, 1431–1442. https://doi.org/10.1175/JAS3917.1

Qiang, X. K., An, Z. S., Song, Y. G., Chang, H., Sun, Y. B., Liu, W. G., et al. (2011). New eolian red clay sequence on the western Chinese Loess Plateau linked to onset of Asian desertification about 25 Ma ago. *Science China Earth Sciences*, *54*(1), 136–144. https://doi.org/10.1007/s11430-010-4126-5

Ramstein, G., Fluteau, F., Besse, J., & Joussaume, S. (1997). Effect of orogeny, plate motion and land-sea distribution on Eurasian climate change over the past 30 million years. *Nature*, *386*, 788–795. https://doi.org/10.1038/386788a0

Rathburn, A. E., Willingham, J., Ziebis, W., Burkett, A. M., & Corliss, B. H. (2018). A New biological proxy for deep-sea paleo-oxygen: Pores of epifaunal benthic foraminifera. *Scientific Reports*, *8*(9456). https://doi.org/10.1038/s41598-018-27793-4

Raymo, M. E., & Ruddiman, W. F. (1992). Tectonic forcing of late Cenozoic climate. *Nature*, *359*(6391), 117–122. https://doi.org/10.1038/359117a0

Razmjooei, M. J., Thibault, N., Kani, A., Ullmann, C. V., & Jamali, A. M. (2020). Santonian-Maastrichtian carbon-isotope stratigraphy and calcareous nannofossil biostratigraphy of the Zagros Basin: Long-range correlation, similarities and differences of carbon-isotope trends at global scale. *Global and Planetary Change*, *184*, 103075. https://doi.org/10.1016/j.gloplacha.2019.103075

Reichart, G. J., Nortier, J., Versteegh, G., & Zachariasse, W. J. (2002). Periodical breakdown of the Arabian Sea oxygen minimum zone caused by deep convective mixing. In P. D. Clift, D. Kroon, C. Gaedicke, & J. Craig (Eds.), The Tectonic and Climatic evolution of the Arabian Sea Region (Vol. 195, pp. 407–419). Geological Society, London, Special Publications. https://doi.org/10.1144/GSL.SP.2002.195.01.22

Reichart, G. J., Schenau, S. J., De Lange, G. J., & Zachariasse, W. J. (2002). Synchroneity of oxygen minimum zone intensity on the Oman and Pakistan Margins at sub-Milankovitch time scales. *Marine Geology*, *185*, 403–438. https://doi.org/10.1016/S0025-3227(02)00563-7

Reuter, M., Piller, W. E., Harzhauser, M., & Kroh, A. (2013). Cyclone trends constrain monsoon variability during late Oligocene sea level highstands (Kachchh Basin, NW India). *Climate of the Past*, *9*, 2101–2115. https://doi.org/10.5194/cp-9-2101-2013

Rosenthal, Y., Field, M. P., & Sherrell, R. M. (1999). Precise determination of element/calcium ratios in calcareous samples using sector field inductively coupled plasma mass spectrometry. *Analytical Chemistry*, *71*(15), 3248–3253. https://doi.org/10.1021/ac981410x

Rothwell, R. G., & Croudace, I. W. (2015). Twenty years of xrf core scanning marine sediments: What do geochemical proxies tell us? In I. W. Croudace, & R. G. Rothwell (Eds.), *Micro-XRF studies of sediment cores: Applications of a non-destructive tool for the environmental sciences* (pp. 25–102). https://doi.org/10.1007/978-94-017-9849-5_2

Scher, H. D., Bohaty, S. M., Zachos, J. C., & Delaney, M. L. (2011). Two-stepping into the icehouse: East Antarctic weathering during progressive ice-sheet expansion at the Eocene–Oligocene transition. *Geology*, *39*(4), 383–386. https://doi.org/10.1130/G31726.1

Schneider, T., Bischoff, T., & Haug, G. H. (2014). Migrations and dynamics of the intertropical convergence zone. *Nature*, *513*, 45–53. https://doi.org/10.1038/nature13636

Schott, F. A., & McCreary, J. P. (2001). The monsoon circulation of the Indian Ocean. *Progress in Oceanography*, *51*(1), 1–123. https://doi.org/10.1016/S0079-6611(01)00083-0

Shenoy, D. M., Suresh, I., Uskaikar, H., Kurian, S., Vidya, P. J., Shirodkar, G., et al. (2020). Variability of dissolved oxygen in the Arabian Sea Oxygen Minimum Zone and its driving mechanisms. *Journal of Marine Systems*, *204*, 103310. https://doi.org/10.1016/j.jmarsys.2020.103310

Spicer, R. A. (2017). Tibet, the Himalaya, Asian monsoons and biodiversity – In what ways are they related? *Plant Diversity*, *39*, 233–244. https://doi.org/10.1016/j.pld.2017.09.001

Srivastava, G., Spicer, R. A., Spicer, T. E. V., Yang, J., Kumar, M., Mehrotra, R., & Mehrotra, N. (2012). Megaflora and palaeoclimate of a Late Oligocene tropical delta, Makum Coalfield, Assam: Evidence for the early development of the South Asia Monsoon. *Palaeogeography, Palaeoclimatology, Palaeoecology*, *342–343*, 130–142. https://doi.org/10.1016/j.palaeo.2012.05.002

Steinthorsdottir, M., Vajda, V., & Pole, M. (2019). Significant transient pCO_2 perturbation at the New Zealand Oligocene–Miocene transition recorded by fossil plant stomata. *Palaeogeography, Palaeoclimatology, Palaeoecology*, *515*, 152–161. https://doi.org/10.1016/j.palaeo.2018.01.039

Stewart, J. A., James, R. H., Anand, P., & Wilson, P. A. (2017). Silicate weathering and carbon cycle controls on the Oligocene–Miocene transition glaciation. *Paleoceanography*, *32*, 1070–1085. https://doi.org/10.1002/2017PA003115

Stewart, J. A., Wilson, P. A., Edgar, K. M., Anand, P., & James, R. H. (2012). Geochemical assessment of the palaeoecology, ontogeny, morphotypic variability and palaeoceanographic utility of *"Dentoglobigerina" venezuelana*. *Marine Micropaleontology*, *84–85*, 74–86. https://doi.org/10.1016/j.marmicro.2011.11.003

Sun, J., Ye, J., Wu, W., Ni, X., Bi, S., Zhang, Z., et al. (2010). Late Oligocene–Miocene mid-latitude aridification and wind patterns in the Asian interior. *Geology*, *38*(6), 515–518. https://doi.org/10.1130/G30776.1

Sun, X., & Wang, P. (2005). How old is the Asian monsoon system? – Palaeobotanical records from China. *Palaeogeography, Palaeoclimatology, Palaeoecology*, *222*, 181–222. https://doi.org/10.1016/j.palaeo.2005.03.005

Super, J. R., Thomas, E., Pagani, M., Huber, M., O'Brien, C., & Hull, P. M. (2018). North Atlantic temperature and pCO_2 coupling in the early–middle Miocene. *Geology*, *46*(6), 519–522. https://doi.org/10.1130/G40228.1

Tada, R., Zheng, H., & Clift, P. D. (2016). Evolution and variability of the Asian monsoon and its potential linkage with uplift of the Himalaya and Tibetan Plateau. *Progress in Earth and Planetary Science*, *3*(4), 1–26. https://doi.org/10.1186/s40645-016-0080-y

Tesfamichael, T., Jacobs, B., Tabor, N., Michel, L., Currano, E., Feseha, M., et al. (2017). Settling the issue of "decoupling" between atmospheric carbon dioxide and global temperature: $(CO_2)_{tm}$ reconstructions across the warming Paleogene–Neogene divide. *Geology*, *45*(11), 999–1002. https://doi.org/10.1130/G39048.1

Thomson, J. R., Holden, P. B., Anand, P., Edwards, N. R., Porchier, C. A., & Harris, N. B. W. (2021). Tectonic and climatic drivers of Asian monsoon evolution. *Nature Communications*, *12*(4022). https://doi.org/10.1038/s41467-021-24244-z

Turner, A. G., & Annamalai, H. (2012). Climate change and the South Asian summer monsoon. *Nature Climate Change*, *2*, 587–595. https://doi.org/10.1038/NCLIMATE1495

van Andel, T. H. (1975). Mesozoic/Cenozoic calcite compensation depth and the global distribution of calcareous sediments. *Earth and Planetary Science Letters*, *26*, 187–194. https://doi.org/10.1016/0012-821x(75)90086-2

van Peer, T., Taylor, V., Liebrand, D., Brzelinski, S., Möbius, I., Friedrich, O., et al. (2020). *Eccentricity-paced ice sheet variability and obliquity-driven bottom-water changes during the Oligocene–Miocene*. Paper presented at European Geosciences Union conference, virtual conference. https://doi.org/10.5194/egusphere-egu2020-15256

Wade, B. S., Berggren, W. A., & Olsson, R. K. (2007). The biostratigraphy and paleobiology of Oligocene planktonic foraminifera from the equatorial Pacific Ocean (ODP Site 1218). *Marine Micropaleontology*, *62*, 167–179. https://doi.org/10.1016/j.marmicro.2006.08.005

Wade, B. S., & Pälike, H. (2004). Oligocene climate dynamics. *Paleoceanography*, *19*, 1–n. https://doi.org/10.1029/2004PA001042

Wade, B. S., Pearson, P. N., Olsson, R. K., Fraass, A. J., Leckie, R. M., & Hemleben, C. (2018). Taxonomy, biostratigraphy, and phylogeny of Oligocene and lower Miocene *Dentoglobigerina* and *Globoquadrina*. In B. S. Wade, R. K. Olsson, P. N. Pearson, B. T. Huber, & W. A. Berggren (Eds.), *Atlas of Oligocene planktonic foraminifera* (pp. 331–384). Cushman Foundation Special Publication No 46.

Webb, A. A. G., Guo, H., Clift, P. D., Husson, L., Müller, T., Constantino, D., et al. (2017). The Himalaya in 3D: Slab dynamics controlled mountain building and monsoon intensification. *Lithosphere*, *9*(4), 637–651. https://doi.org/10.1130/L636.1

Wei, H. H., & Bordoni, S. (2016). On the role of the African Topography in the South Asian Monsoon. *Journal of the Atmospheric Sciences*, *73*, 3197–3212. https://doi.org/10.1175/JAS-D-15-0182.1

Westerhold, T., Marwan, N., Drury, A. J., Liebrand, D., Agnini, C., Anagnostou, E., et al. (2020). An astronomically dated record of Earth's climate and its predictability over the last 66 million years. *Science*, *269*, 1383–1387. https://doi.org/10.1126/science.aba6853

Wright, J. D., Miller, K. G., & Fairbanks, R. G. (1992). Early and middle Miocene stable isotopes: Implications for deepwater circulation and climate. *Paleoceanography*, *7*(3), 357–389. https://doi.org/10.1029/92pa00760

Xie, S. P., Xu, H., Saji, N. H., Wang, Y., & Liu, W. T. (2006). Role of narrow mountains in large-scale organization of asian monsoon convection. *Journal of Climate*, *19*, 3420–3429. https://doi.org/10.1175/jcli3777.1

Yang, F., Kumar, A., Schlesinger, M. E., & Wang, W. (2003). Intensity of hydrological cycles in warmer climates. *Journal of Climate*, *16*, 2419–2423. https://doi.org/10.1175/2779.1

Yang, X., Groeneveld, J., Jian, Z., Steinke, S., & Giosan, L. (2020). Middle Miocene intensification of South Asian monsoonal rainfall. *Paleoceanography and Paleoclimatology*, *35*, 1–18. https://doi.org/10.1029/2020PA003853

Young, J. R. (1998). Neogene Nannofossils. In P. R. Bown (Ed.), *Calcareous nannofossil biostratigraphy* (pp. 225–265). Kluwer Academic. https://doi.org/10.1007/978-94-011-4902-0_8

Yu, Z., Colin, C., Wan, S., Saraswat, R., Song, L., Xu, Z., et al. (2019). Sea level-controlled sediment transport to the eastern Arabian Sea over the past 600 kyr: Clay minerals and Sr–Nd isotopic evidence from IODP site U1457. *Quaternary Science Reviews*, *205*, 22–34. https://doi.org/10.1016/j.quascirev.2018.12.006

Zachos, J. C., Breza, J. R., & Wise, S. W. (1992). Early Oligocene ice-sheet expansion on Antarctica: Stable isotope and sedimentological evidence from Kerguelen Plateau, southern Indian Ocean. *Geology*, *20*, 569–573. https://doi.org/10.1130/0091-7613(1992)020<0569:eoiseo>2.3.co;2

Zachos, J. C., Flower, B. P., & Paul, H. (1997). Orbitally paced climate oscillations across the Oligocene/Miocene boundary. *Nature Letters*, *388*, 567–570. https://doi.org/10.1038/41528

Zachos, J. C., & Kump, L. R. (2005). Carbon cycle feedbacks and the initiation of Antarctic glaciation in the earliest Oligocene. *Global and Planetary Change*, *47*, 51–66. https://doi.org/10.1016/j.gloplacha.2005.01.001

Zachos, J. C., Quinn, T. M., & Salamy, K. A. (1996). High-resolution (10^4) deep-sea foraminiferal stable isotope records of the Eocene–Oligocene transition. *Paleoceanography*, *11*(3), 251–266. https://doi.org/10.1029/96PA00571

Zachos, J. C., Shackleton, N. J., Revenaugh, J. S., Palike, H., & Flower, B. P. (2001). Climate response to orbital forcing across the Oligocene–Miocene boundary. *Science*, *292*, 274–278. https://doi.org/10.1126/science.1058288

Zeebe, R. E., & Tyrrell, T. (2019). History of carbonate ion concentration over the last 100 million years II: Revised calculations and new data. *Geochimica et Cosmochimica Acta*, *257*, 373–392. https://doi.org/10.1016/j.gca.2019.02.041

Zhang, T., Han, W., Fang, X., Song, C., Wang, Y., Tian, Q., et al. (2021). Tectonic forcing of environmental transition in Central Asia at ~11–9 Ma. *Gondwana Research*, *89*, 19–30. https://doi.org/10.1016/j.gr.2020.08.012

Zhang, Y. G., Pagani, M., Liu, Z., Bohaty, S. M., & Deconto, R. (2013). A 40-million-year history of atmospheric CO_2. *Philosophical Transactions of the Royal Society A*, *371*, 1–20. https://doi.org/10.1098/rsta.2013.0096

Zheng, H., Wei, X., Tada, R., Clift, P. D., Wang, B., Jourdan, F., et al. (2015). Late Oligocene–early Miocene birth of the Taklimakan Desert. *Proceedings of the National Academy of Sciences of the United States of America*, *112*(25), 7662–7667. https://doi.org/10.1073/pnas.1424487112

References From the Supporting Information

Bevington, P. R., & Robinson, K. D. (2003). *Data reduction and error analysis for the physical sciences* (3rd ed.): McGraw-Hill.

Parsons, B., & Sclater, J. G. (1977). An analysis of the variation of ocean floor bathymetry and heat flow with age. *Journal of Geophysical Research*, *82*(5), 803–827.

Routledge, C. M., Kulhanek, D. K., Tauxe, L., Scardia, G., Singh, A. D., Steinke, S., et al. (2020). A revised chronostratigraphic framework for International Ocean Discovery Program Expedition 355 sites in Laxmi Basin, eastern Arabian Sea. *Geological Magazine*, *157*, 961–978.

Sclater, J. G., Meinke, L., Bennett, A., & Murphy, C. (1985). The depth of the ocean through the Neogene. In J. P. Kennett (Ed.), *The Miocene ocean: Paleoceanography and biogeography* (pp. 1–21). Geological Society of America, Memoir 163.

Straume, E. O., Gaina, C., Medvedev, S., & Nisancioglu, K. H. (2020). Global cenozoic paleobathymetry with a focus on the Northern Hemisphere Oceanic Gateways. *Gondwana Research*, *86*, 126–143. https://doi.org/10.1016/j.gr.2020.05.011